Plasmon polariton Bragg gratings and IR-140 doped PMMA for active Bragg structures

Maude Amyot-Bourgeois

A thesis submitted to the Faculty of Graduate and Postdoctoral Studies in partial fulfillment of the requirements for the degree of

Master of Science
in Physics

Ottawa-Carleton Institute for Physics
University of Ottawa
Ottawa, Canada

Abstract

This thesis contributes to the realisation of plasmonic lasers based on plasmon polariton Bragg gratings. The scope of this thesis is twofold. In the first section, entitled *Passive plasmonic Bragg grating characterization*, the results of the testing and characterization of a new design of plasmonic Bragg gratings in the near-infrared are presented. The reflection and transmission responses expected from plasmon-polariton Bragg gratings (PPBGs) are treated theoretically using the transfer matrix method (TMM) and the numerical model is validated experimentally. The experimental setup and procedures are then described in detail. Results show that the near-infrared plasmon polariton Bragg gratings possess a Bragg reflection at a wavelength close to the Bragg wavelength predicted by TMM. In the second section, *Gain optimisation and bleaching of IR-140 doped PMMA*, an in-depth analysis of the gain medium (IR-140 dye doped poly(methyl methacrylate) better known as PMMA) is performed. This gain medium was selected as a gain layer for active plasmonic gratings and distributed feedback lasers designed by a colleague Ph.D. candidate. The optimized molecular weight of IR-140 in PMMA was found to be 0.9% to obtain a material gain of 81 cm^{-1}.

Acknowledgments

I would like to thank my supervisor, Dr. Pierre Berini, for all his help and guidance throughout this thesis research. I would also like to thank him for the financial support provided during the entire period of my thesis.

I am very grateful for Elham Karami Keshmarzi for the fabrication of the devices analysed in my thesis, as well as for her assistance and guidance always provided with such kind heart. Her friendship is precious to me.

A very special thanks to Anthony Olivieri for his long lasting support with anything technical related to laboratory work. His patience and availability were much appreciated.

I want to thank all my other colleagues in the laboratory for their friendship and their help. Their presence made these two years a very pleasant time.

Lastly, I want to thank my husband, Philippe, and my family for their unconditional love and support.

Nomenclature, Acronyms and Symbols

Latin letters and Acronyms

ASE	Amplified Spontaneous Emission
Au	gold
c	speed of light
CF	Confinement Factor
CW	Continuous Wave
DFB	Distributed FeedBack
DUT	Device Under Test
E	Electric field
FEM	Finite Element Method
FWHM	Full-Width-Half-Maximum
g	gain
H	magnetic field
i	element number in an ensemble
I	Intensity
ICCD	Intensified Charge-Coupled Device
L	Length
laser	Light Amplification by Stimulated Emission of Radiation
LRSPP	Long-Range Surface Plasmon
MMF	Multi-Mode Fibre
MoL	Method of Line
MPA	Mode Power Attenuation
MPG	Mode Power Gain
m.w.	molecular weight
n	refractive index
N	Number of unit cells in a Bragg
Nd:YAG	Neodymium-Doped Yttrium Aluminum and Garnet laser
P	Power [Watt]
PM	Polarisation Maintaining
PMMA	poly(methyl methacrylate)
PPBG	Plasmon Polariton Bragg Grating
R	Reflection
SE	Spontaneous Emission
Si	Silicon
SiO_2	Silica
SP	Surface Plasmon
SPP	Surface Plasmon Polariton
SW	Straight Waveguide
t	thickness
T	Transmission
TE	Transverse Electric
TM	Transverse Magnetic
TMM	Transfer Matrix Method
VSL	Variable Slit Length method
w	width

Greek letters

α	Attenuation Constant
ϵ	Dielectric Constant
θ	Incident beam angle
λ	Wavelength
Λ	Pitch
ω	Angular Frequency

Subscripts

ave	average
B	Bragg
b	bound
i	incident (right-propagating) or element number i^{th}
mat	material
mod	modal
p	pump
r	reflected (left-propagating)

List of Figures

(From publication)

List of Tables

Table of Contents

Chapter 1: Introduction and Literature Review

1.1 Introduction to plasmonics

Electromagnetic waves supported at the interface between two media are called surface modes. These electromagnetic (EM) radiations can couple to collective plasma oscillations (oscillating dipoles formed by the excited conduction electrons, with the positive charge of the ion core). This coupling of the EM field to the plasmons (quantum particles of the plasma oscillations) can only happen for wave frequencies ω smaller than the plasma frequency ω_p otherwise the waves incident do not propagate and are reflected [1]. If $\omega<\omega_p$, then coupling between the photons and the plasmons is allowed to generate plasmon-polaritons, which are hybrid waves propagating along an interface between two media. If the two media have their real part of the electrical permittivity of opposite signs, they can support surface modes called *surface plasmon-polaritons* (SPPs). This opposite sign of dielectric constant occurs, for example, for a metal (gold, silver) having a negative real dielectric constant, and a dielectric such as silica, with positive real dielectric constant, at optical wavelengths. Such a situation is represented in Figure 1 as a single interface between a metal and a dielectric, supporting SPP waves. These waves propagating along the interface are generated by the coupling of the electromagnetic (EM) field to the dipole at the surface of the metal, formed by the excited surface electrons named a *surface plasmon*. SPP waves are transverse magnetic (TM) in nature, which means that only 3 of the 6 field components are supported (E_y, E_z and H_x from Figure 1 geometry) and no transverse electric (TE) polarised wave is supported in a structure such as the one represented in Figure 1. SPP waves are tightly confined to the metal-dielectric interface and the mode becomes evanescent in the dielectric far from the interface.

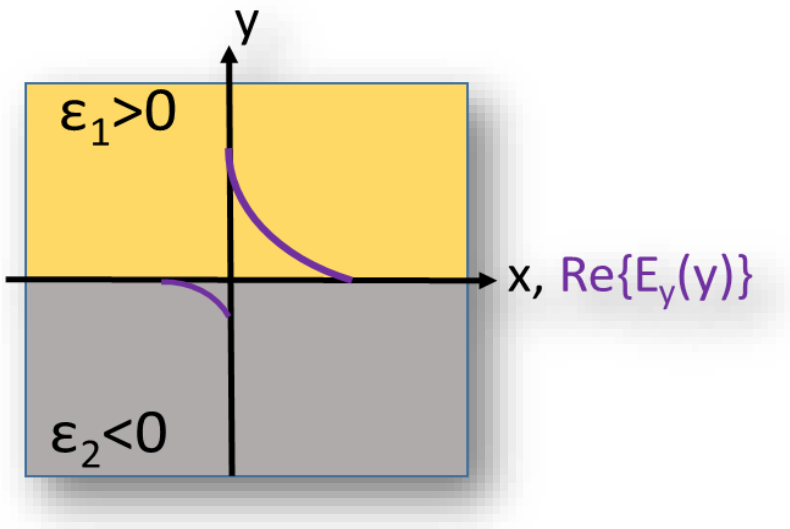

Figure 1 Single interface structure supporting SPP waves, made by a metal (grey) and a dielectric (yellow). In purple is the real part of the E_y dominant component as a function of y, propagatin in the x-z plan. The real part of the permittivity Re{ε} is shown. The z-axis is pointing out of the screen.

A structure of interest is the case of a metallic film of infinite width, bounded by two dielectric materials of the same permittivity ($\varepsilon_1=\varepsilon_3$). If the thickness of the metal (see Figure 2) is quite large, the top and bottom interfaces each act as the single interface situation. As the metal thickness decreases, coupling (through tunneling) between the top and bottom SPP bounded to each interface increases until the metal is thin enough so that supermodes are created [2]. Two main supermodes are thus created termed symmetric s_b (the field components are symmetrical along the y axis, shown in Figure 2) and asymmetric a_b. The symmetric mode shows the interesting property of a decreasing attenuation constant (and an increased propagation length) as the thickness is reduced, due to increased penetration into the dielectric background which possesses practically no loss. They are thus called *long-range* SPPs. The asymmetric mode a_b is called short-range SPP (SRSPP) because, unlike the s_b mode, its attenuation is quite high. Both modes are represented in purple lines, in Figure 2. As the metal thickness approaches zero, the TM mode evolves into a TEM mode that is allowed

to propagate in the cladding. There is therefore less confinement to the metal slab as the thickness is decreased, causing a trade-off between confinement and loss.

Although the low loss properties of the LRSPP waves in the metallic slab can seem attractive, this structure is of little interest due to its 1D confinement. Indeed, the wave propagates laterally and is only confined along the y axis shown on Figure 2, illustrated by the sketches of the y components of electric field as a function of y.

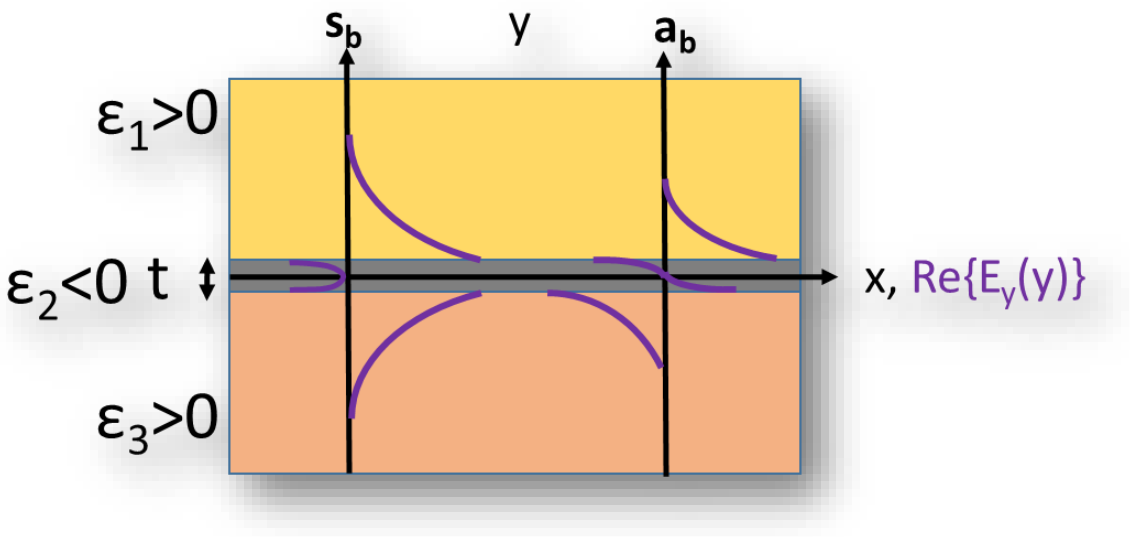

Figure 2 Metallic slab of infinite width in x and z, bounded by two dielectric layers (all parameters assumed to be real on the schematic), t is the metal thickness and the purple lines represent the dominant electric field in y component $E_y(y)$

The structure now evolves from the slab metallic film into a structure with a metallic stripe of finite width (as seen in Figure 3 and Figure 4) with a width to thickness ratio w/t>>1. This finite width configuration provides 2D confinement, not possible with the slab structure, allowing for waveguide applications. Multiple modes are supported in this structure, such as bound modes, leaky modes and higher order modes, but we are interested in the bound modes only. Unlike SPP waves supported by the slab which were purely TM, these modes in the finite width structure have all six field components,

but the electric field component perpendicular to the interface strongly dominates [2]. For a thick metal film, all modes are confined to the corners of the metallic stripe and no coupling between the modes at the interfaces occurs. The bound mode of interest has symmetric fields along x and y as seen in Figure 3 (z being the direction of propagation) as it follows the same pattern as the symmetric bound mode in the slab metallic waveguide for a decreasing metallic thickness: as the two SPP waves at the top and bottom interfaces couple to each other, they evolve into a Gaussian-like field distribution (with an extremum at the centre of the stripe) [3]. The attenuation constant decreases dramatically with decreasing thickness because the modes lose confinement to the stripe, and become supported by the background dielectric which has very low loss. The SPP modes can then travel to longer distance, thus called *long-range* SPP (LRSPP). As the thickness decreases even more, the LRSPP loses its confinement. There is therefore a trade-off between loss and confinement. These LRSPP modes can be used for many integrated optical applications since, unlike the LRSPP mode of the slab waveguide, they possess good 2D confinement in addition to showing low loss.

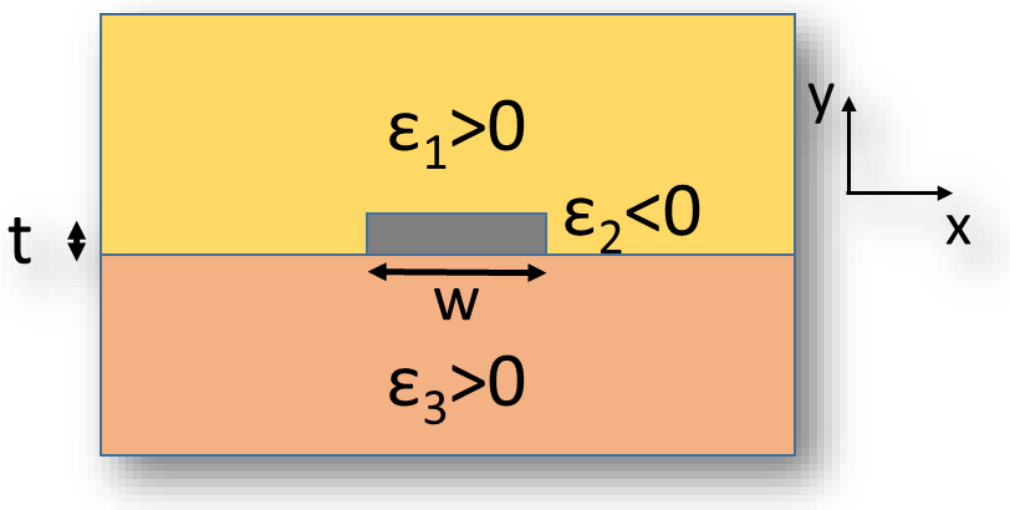

Figure 3 Metallic stripe of finite width w and thickness t bounded by two dielectrics. All dielectric constants shown are the real part. The x-y coordinate is shown and the waves propagate along the z direction.

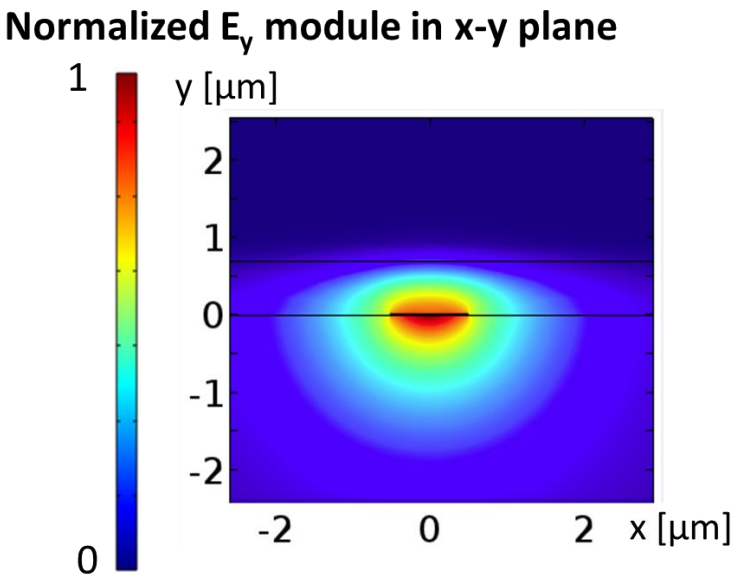

Figure 4 Normalized electric field profile of the ss_b^0 (symmetric) mode of a cross sectional area of an asymmetric structure in the x-y plane for a thin gold stripe (t=20 nm) with finite width (1 μm) bound by PMMA and silica

In the case of slightly inhomogeneous dielectric cladding structure, which means when $\varepsilon_1 \neq \varepsilon_3$ on Figure 3, but Δn ($\Delta n = n_3 - n_1$ is the real refractive index difference between the claddings 1 and 3) is smaller than 0.1 [4] the bound modes are not localized symmetrically at the two interfaces. Instead, they will be more strongly localized in the lower or higher real dielectric constant medium, depending if their electric field component is symmetric or asymmetric [4]. There exists a cut-off metal thickness limit after which no LRSPP mode is supported due to the complete loss of confinement (and LRSPP modes cannot be exclusively supported by the dielectric cladding) but the interesting properties of the LRSPP modes, such as the reduced attenuation constant and confinement, start showing up for the bound symmetric mode at a metal thickness quite close to the cutoff thickness, resulting in small fabrication tolerance.

SPPs are used in many fields of optics due to their interesting properties. Localized SPP can have a mode size lower than the diffraction limit. The strong SPP mode confinement is of interest in non-linear optics and nanophotonics. This strong

confinement also leads to a field enhancement [5]. This effect is exploited in fields such as spectroscopy (one good example being the surface-enhanced Raman scattering) or non-linear optics. Ghamsari and colleagues [6] used the resonant enhancement properties of SPPs on nanoantennas on graphene for Raman scattering enhancement (registering a scattering cross-section gain of 160) and demonstrated that it is based on enhanced resonant Stokes emission by monopole gold nanoantennas. SPP high sensitivity to the bounding dielectric media makes it attractive for biosensing applications. Krupin and colleagues [7] designed and tested a structure supporting LRSPP, made of 5 µm wide 22 nm thick gold stripes bounded on the bottom by Cytop (a known amorphous fluoropolymer) and on top by microfluidic channels injected with solutions of various refractive index, as seen in Figure 5. Because of the high LRSPP sensitivity to bulk refractive index, this structure allowed measurements accuracy of the refractive index down to $2x10^{-6}$. This method allows the detection of cells based on type, and of proteins for disease detection [8,9,10,11].

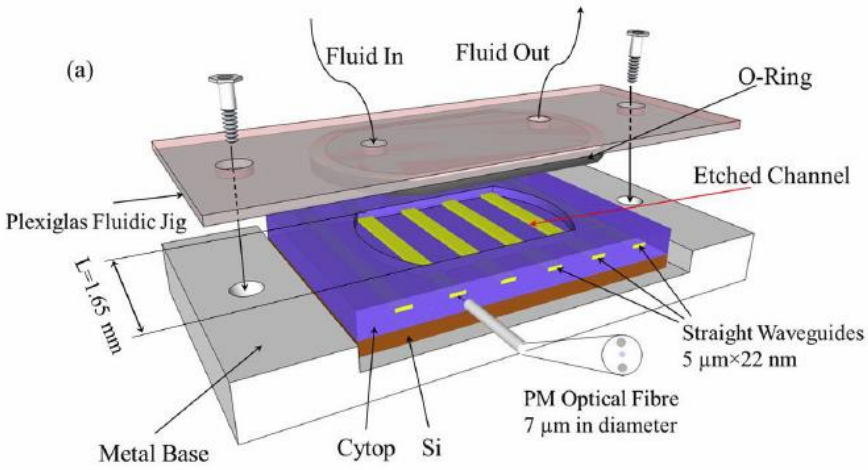

Figure 5 Microfluidic channel chip for biosensing applications. Adopted from Ref. [7], Copyright (2013), with permission from OSA.

1.2 Plasmon polariton Bragg gratings

One of the interesting applications of plasmonics are plasmon polariton Bragg gratings (PPBGs). These can be used as high reflection structures for LRSPPs and their

high performance makes them attractive as the resonator section for plasmonic lasers. Before going into details on PPBG characteristics, fundamental concepts will be explained.

1.2.1 Gratings

Most physicists are familiar with the diffraction grating. It is a periodic arrangement of fine lines (opaque on transparent surface, or fine apertures on opaque material), with sizes comparable to the wavelength of the light incident on the grating. The grating characteristics will have an impact on the intensity and phase of the light transmitted through the grating [12]. The interference figure obtained on a screen at a certain distance from the diffraction grating depends on the aperture width, the distance between each aperture, the optical wavelength and the distance between the screen and the grating.

1.2.2 Bragg gratings and dielectric Bragg gratings

Bragg gratings are periodic arrangements of N planar semi-transparent mirrors, allowing for wavelength tunability and incident angle selection [13]. The length of a unit cell comprised of two layers is called the pitch Λ and the duty cycle (dc) of a grating is the ratio between the two section lengths: dc=100%*d_1/Λ, where d_1 is the length of section 1.

Dielectric Bragg gratings are stacks of double layer cells made of two segments with thickness and refractive index d_1, n_1 and d_2, n_2. The total phase induced by a round-trip in a unit cell (propagating through section 1 and 2 in the forward and backward directions) is:

$$\varphi_1 + \varphi_2 = k_0(n_1 d_1 + n_2 d_2) \qquad (1)$$

where k_0 is the free space wavevector. The peak reflectance of this structure (when the reflected wave intensity is at its maximum) will satisfy the Bragg condition stating that $2(\phi_1+\phi_2) = 2\pi q$ (q being a positive integer). Figure 6 shows a simple representation of a dielectric Bragg. One can calculate the reflectance and transmittance of such a grating using the transfer matrix method (TMM) explained in a subsequent section.

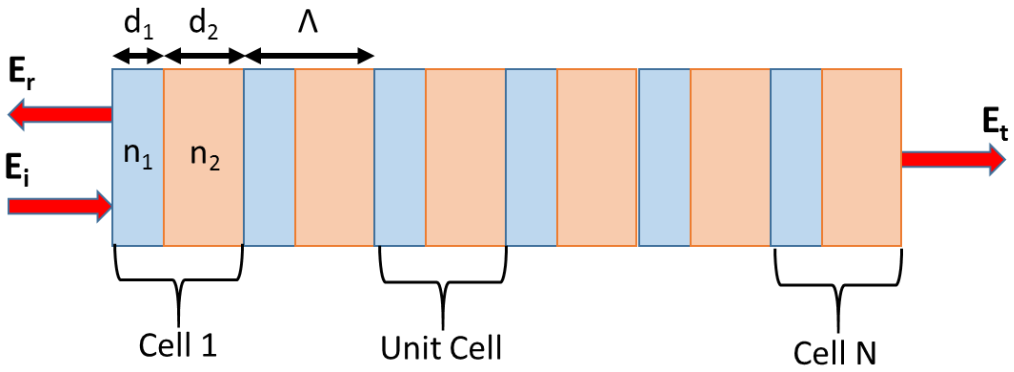

Figure 6 Drawing of dielectric Bragg grating made of N unit cells with sections 1 and 2. Incident (i), reflected (r) and transmitted (t) electric fields are represented.

A Bragg grating made of periodic layered media can be designed in such a way that it will possess forbidden wave bands of transmission at which a wave cannot propagate into the grating. These are called Bragg reflectors and they exhibit high reflectance [14]. As the number of cells N increases, the reflectance at resonance approaches 1. At normal incidence, the resonance wavelength λ_B derived from the Bragg condition and equation 1 is given by:

$$\lambda_B = \frac{2*n_{ave}*\Lambda}{O} \qquad (2)$$

where n_{ave} is the average refractive index of sections 1 and 2 and *O* is the grating order. A specific case of high-reflectance Bragg reflectors is a periodic stack of layers with a thickness measuring a quarter of a wavelength, $n_1d_1=n_2d_2=\lambda/4$. The reflectance response

in Figure 7 has been calculated using the TMM. The graph shows information characteristic to Bragg gratings, such as the maximum reflection R=0.9993, the Bragg wavelength λ_B =910 nm, the FWHM (bandwidth) $\Delta\lambda_B$ =14.4 nm and the sidelobes (usually undesired).

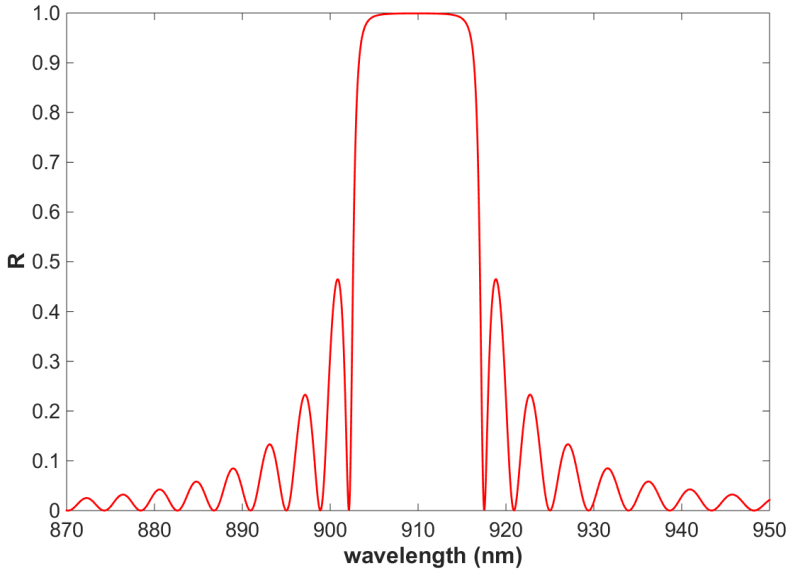

Figure 7 Reflectance response for a dielectric Bragg grating made of silica and PMMA, calculated grating has a number of periods N=200, d_1=155 nm and d_2=152 nm.

1.2.3 Plasmon Polariton Bragg Gratings (PPBGs)

Bragg gratings supporting LRSPP waves are called plasmon polariton Bragg gratings (PPBGs). The basic structure of the PPBG, as the waveguide structure for long range SPP, is a metallic stripe of finite width bounded by two dielectric claddings (homogeneous or inhomogeneous), thin enough so that the SPP modes at the two metal-dielectric interfaces can couple together to form the LRSPP wave. The Bragg grating is generated from a periodic perturbation of a parameter along the waveguide. This perturbation between each section of the waveguide induces a partial reflection at each interface. As for dielectric Bragg grating, the resonance wavelength that has maximum reflection from constructive addition of all partial reflections is determined by the Bragg condition [15]. Many parameters can be varied to generate the grating perturbation. Bozhevolnyi and colleagues [16] fabricated and tested a Bragg grating

supporting LRSPP waves constructed as a concatenation of metal sections with a modulated metal thickness. The waveguide stripe was gold, with width w=8 μm and reference thickness t=15 nm. The gold stripe was embedded in a dielectric consisting of benzocyclobutene (BCB) polymer. The metal ridge varied by a height Δt=10 nm or higher, and the grating had a periodicity Λ=500 nm. The experiment consisted of coupling a probe signal from a broad-band source (EE-LED diode, λ=1500-1600 nm) to the waveguide via end-fire coupling. The reflectance (R) and transmittance (T) spectra were obtained and normalized to a straight waveguide, used as reference calibration. The grating bandgap was found to be at λ_B=1550 nm and the dip (for T) and peak (for R) bandwidth was $\Delta\lambda_B$=20 nm. The R and T spectra were compared for various ridge heights, and it was found that for a ridge higher than 30 nm, the R and T spectra would become distorted, believed to be due to out-of-plane scattering.

Since LRSPP modes are mostly confined in the dielectric layers, the mode effective index is very dependent on the refractive index of these two cladding layers. Nevertheless, a modification of the metal cross section between each section (as the stripe width) can have mild influence on the LRSPP effective mode index. Jetté and Berini [17] proposed a Bragg grating design supporting LRSPP waves, made of periodic sections of different width. The grating performance was explored theoretically, using the transfer matrix method (TMM) applied to a dielectric stack model of the structure, which is a very simple and general method to treat this situation. They explored three different Bragg designs: a uniform periodic Bragg grating; an interleaved grating (a supergrating made of the concatenation of supercells containing two different gratings) and an apodized grating. All waveguides consisted of a gold stripe with a thickness t=20 nm and a certain width determining its effective refractive index, obtained from method of lines (MoL) calculations and Maxwell's equations for each specific geometry. The stripe was on a silica substrate and the top layer was an index matching polymer, making this structure symmetrical. The uniform periodic design had a wide section with width w_1=8 μm, and a short section with width w_2=2, 3 or 4 μm. The first order gratings

had a pitch Λ=536 nm and dc=50% while the third order had a pitch Λ=1.6 µm and dc=50%. The grating length was varied by increasing the number of unit cells. The R and T curves obtained from the TMM simulation showed that the Bragg response (R peak and T dip, at a Bragg wavelength λ_B=1548 nm) increases as Δw (w_1-w_2) increases. Also, the bandwidth narrows as Δw increases. The first order grating had a stronger response than the third order, with a reflection peak R_1=0.935 while R_3=0.77 for a similar Δw. The interleaved Bragg design consisted of a grating made of many supercells, each with section w_{1A}=8 µm, w_{2A}=2 µm, w_{1B}=8 µm, w_{2B}=2 µm, d_A=268 nm and d_B=269 nm. The interleaving design provides tuning of the Bragg wavelength. This new design had a Bragg wavelength λ_B=1551.45 nm and a reflection peak comparable to the uniform periodic grating. The apodized design, consisting of a sinusoidal variation in the width modulation, was intended to reduce the sidelobes surrounding the main peaks and dips in the spectra. The results showed a significant reduction in the sidelobes although accompanied by a weaker reflection coefficient (peak R=0.805).

In a subsequent publication [18], Jetté and colleagues proceeded to test experimentally the uniform periodic grating previously studied via TMM. They added a fourth Δw iteration to their fabricated gratings, where the width of the second section is w_2=0 µm (essentially a metallic gap). All gratings had a third order periodicity for ease of fabrication. The gratings were probed with a tunable laser coupled via end-fire coupling technique, which is a coupling technique that uses a polarisation-maintaining (PM) fibre to match the mode exiting the fibre into the LRSPP modes supported by the grating while minimising coupling loss due to mode mismatch or misalignment. The experimental setup is shown in Figure 8. The resulting T and R spectra showed that off-resonance ($\lambda \neq \lambda_B$) T decreases as the grating length L_G increases, due to an increase in propagation loss but the on-resonance T dip ($\lambda = \lambda_B$) decreases even more owing to a stronger grating. The refectance peak also increases with L_G. The T curve also showed an asymmetry in the transmission between the left and right side of the dip at λ_B, shorter wavelengths exhibiting lower T attributable to a higher coupling into the radiative modes, or more scattering. The TMM study showed that R increased with L_G and Δw.

The grating showing the best performance was the gap grating, and L_G=4.5 mm, its reflection peak R=-1.8 dB, representing a 66% reflection of the input wave. Jetté and colleagues [15] compared results obtained numerically (TMM) and experimentally, as shown in Figure 9. They noted an average difference of 30% between the T dips obtained from TMM and from experiment, the TMM dips being the deepest, although R peaks agreed within 10% between TMM and experiment. The measured Bragg wavelength λ_B=1544.2 nm was found to be 1.6 nm higher than the numerical Bragg wavelength (λ_B=1542.6 nm). It was attributed to an unwanted non-uniform pattern in the Bragg gratings. They performed some tolerance tests numerically to explain this phenomenon and concluded that it was explained by a discrepancy between the targeted pitch and the effective grating pitch.

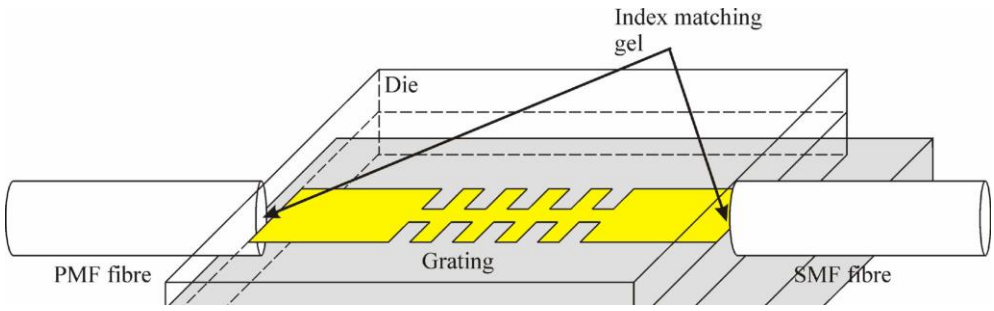

Figure 8 Experimental setup used to test PPBGs for telecommunication wavelengths
Adopted from Ref. [18], Copyright (2005), with permission from OSA.

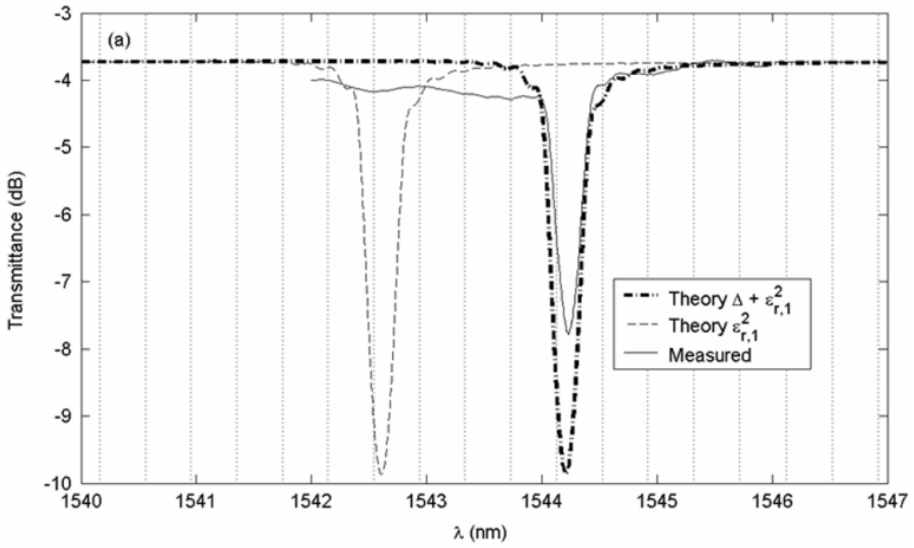

Figure 9 Comparison between theoretical and experimental transmittance of PPBGs for telecommunication wavelengths [15] © 2005 IEEE

1.3 Loss compensation of LRSPP by optical amplification

Even though LRSPP waves have longer propagation lengths and lower attenuation than SRSPP and SPP on a single interface, the losses encountered are still high, and the propagation length expected is measured in terms of millimetres to centimetres only. This high propagation loss is a strong limitation to the application of LRSPP in many fields. The losses due to energy dissipation become even more important in the visible and NIR regime, as seen from the complex permittivity dependence on the wave angular frequency ω, given by the Drude model. A LRSPP wave propagating in the +z direction would have an electric field with a complex phase dependence of the form *exp[(iβ-α)z]* where β is the phase constant and α is the attenuation constant, used to calculate the propagation length (distance travelled by a wave before most of its power is dissipated) $L_\alpha = 1/(2\alpha)$ [19]. The attenuation constant, calculated in rad/m, is quite high (few hundreds) and affects the power output from a LRSPP waveguide according to this equation [20]:

$$P_{out} = P_{in} C_{in} C_{out} e^{-2\alpha L} \qquad (3)$$

where P_{out} and P_{in} are respectively the output and input power of the waveguide, C_{in} and C_{out} are the input and output coupling loss factors of the mode into and out of the waveguide and L is the waveguide length. The mode power attenuation MPA (in dB/mm) can be derived from this equation:

$$MPA = \left(\frac{20}{1000}\right)\alpha log_{10}e \qquad (4)$$

It is interesting to introduce gain to overcome loss in the waveguide and obtain mode power gain (MPG). The manner to obtain modal gain and SPP amplification is to have a positive *exp(αz)* dependence of the electric field. A solution to this attenuation problem came from Sudarkin and colleagues [21] who proposed the addition of a pumped gain material in one of the dielectric layers bounding the metal film to increase the propagation length from a population inversion in the gain material, thus creating a doped dielectric medium. For optical pumping, covalent or ionic solids that are transparent are good hosts for dye molecules as long as solvent compatibility and solubility issues pertaining to the dye and host molecules can be resolved. The pump radiation is absorbed by the ground state dye molecules. The excited molecules might decay into any of the multitude of existent optical modes, from spontaneous emission, but if a waveguide mode is present, then mode photons stimulate the emission of duplicate photons at the same wavelength into the mode. This process is called stimulated emission [13]. Another decay process, called amplified spontaneous emission (ASE) arises from spontaneous radiation in an amplifier waveguide mode that is then amplified by the gain material (due to stimulated emission). Therefore, the spontaneous emission intensity grows as the wave travels along the length of the amplifier axis according to this equation [13]:

$$\frac{dI}{dz} = g_{mod}I + J_{sp} \qquad (5)$$

where g_{mod} is the modal gain in the doped medium and J_{sp} is a term related to the spontaneous emission rate. This amplified spontaneous emission phenomenon causes a spectral narrowing in the emission spectrum due to the stimulated amplification. It is also strongly directional, as it follows the shape of the amplifier region [22]. ASE is undesirable in a laser amplifier medium, as it depletes the population of the excited state, and is in competition with the lasing mode for available gain.

The small signal gain coefficient α_e for a doped dielectric gain medium is given by [19]:

$$\alpha_e = N \frac{I_p \tau \sigma_p \sigma_e - \sigma_a \hbar \omega_p}{\hbar \omega_p + I_p \tau \sigma_p} \qquad (6)$$

where N represents the molecular density, τ is the excited-state lifetime, σ_p, I_p and ω_p are the absorption cross section, intensity and angular frequency of the pump signal and σ_e is the emission cross section. This theoretical calculation of the small signal gain coefficient is used to obtain a calculated value of the gain medium's relative complex dielectric constant, used later for modal analysis [19]:

$$\epsilon_{r,e} = \epsilon_{r,e\ passive} + i \frac{\lambda_e}{2\pi} \alpha_e \sqrt{\epsilon_{r,e\ passive}} \qquad (7)$$

where $\epsilon_{r,e\ passive}$ is the undoped (passive, as oppose to active) cladding dielectric relative permittivity. This material specification along with material specifications of the entire structure (geometry and optical characteristics) are input parameters for a mode analysis of the SPP mode, from numerical techniques such as the method of lines (MoL) or the finite element method (FEM). The result of interest from such a numerical analysis is the complex mode effective index. From that, one can extract the real part of the propagation constant, Re{k}=α, which will be positive in the case of amplification and negative for attenuation. The gain coefficient is then calculated as $g=2\alpha$ (the factor 2 is because power has a $exp(2\alpha z)$ dependence, as P comes from the norm of the

electric field E) the mode power gain obtained from the pumped waveguide segment is $MPG=20log_{10}e\alpha$ [23].

LRSPPs have a lower attenuation constant [4] because as the metal thickness decreases, the mode confinement also decreases and the LRSPP mode evolves from a purely TM mode into a TEM-like mode (but with TM components of the 6 vector fields being dominant) with its mode field decaying into the lossless dielectric medium [5]. Because of this, the amount of gain needed to compensate the loss in LRSPP is smaller than other types of SP waves [23], but many investigations have been conducted on the stimulated emission and amplification of localized SP and propagating SPP waves by optically pumping an adjacent gain medium.

Seidel and colleagues [24] demonstrated loss compensation of SPPs at the interface between a metallic film and an amplifying dielectric. The structure under test was a thin silver film (t=100 nm) coated by a dye (rhodamine 101 or cresyl violet) in ethanol solution, in a Kreschmann-Raether configuration (shown in Figure 10). The probe signal was from a dye laser emitting at λ_{probe}=580 nm and the gain layer was pumped with a HeNe laser λ_{pump}=633 nm. Stimulated emission into SPPs was observed as an increase in the intensity of the reflected probe light from the prism.

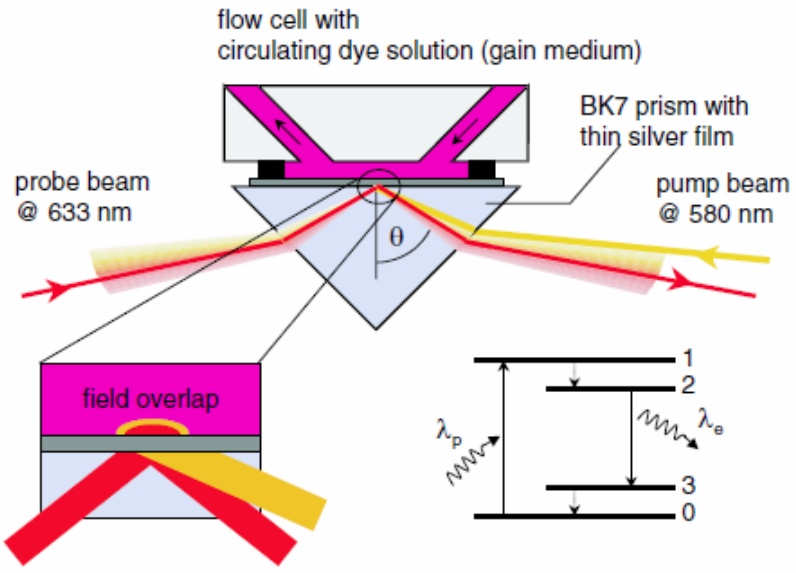

Figure 10 Schematic of the Kretschmann-Raether experimental setup and 4-level representation of the dye molecule interaction with radiation [24] © 2005, American Physical Society

Grandidier and colleagues [25] could obtain partial loss compensation of SPPs in a dielectric strip made of poly(methyl methacrylate) (PMMA) doped with nanocrystals consisting of lead sulphide (PbS), deposited on a metal film made of gold, of a 40 nm thickness, shown in Figure 11. The probe signal used to couple to SPP waves supported in this structure was emitting at λ_{probe}=1550 nm while the quantum dots (QDs) formed by the nanocrystals were pumped at λ_{pump}=532 nm and the pump intensity was varied. The SPP propagation length L_{SPP} was obtained from the intensity distribution and it was found that the pumping had caused a 27% increase in the L_{SPP}. Although no spectral narrowing could be confirmed due to experimental limitations, the signal emitted was proved to be SPP due to the narrowing of the effective refractive index distribution in momentum space.

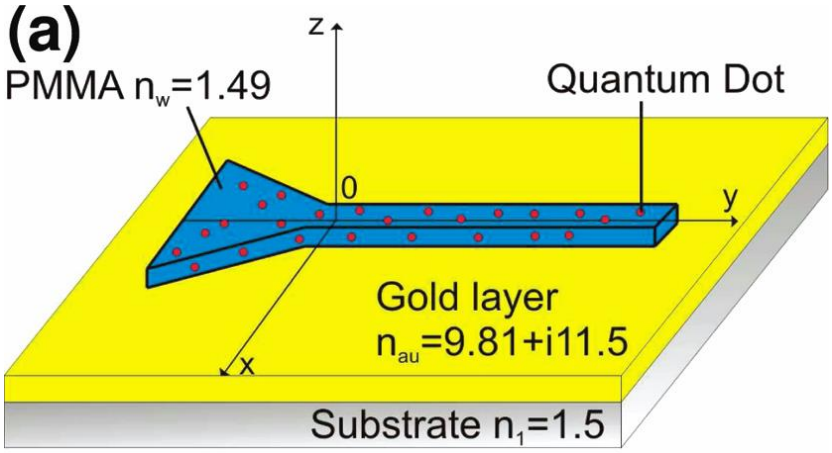

Figure 11 Schematics of the dielectric-loaded SPP waveguide [25]. Reprinted (adapted) with permission from (Grandidier, J., Colas des Francs, G., Massenot, S., Bouhelier, A., Markey, L., Weeber, J.-C., . . . Dereux, A. (2009). Gain-Assisted Propagation in a Plasmonic Waveguide at Telecom Wavelength. Nano Letters **9**, *2935). © (2009) American Chemical Society.*

Bolger and colleagues [26] suspected that a limitation to the full compensation of the attenuation by an amplifier is due to the competition of SPP-ASE and the amplified input SPP, thus reducing the available gain for total compensation of the SPP propagation losses. The structure under test was a gold film (t=100 nm) deposited on a silica substrate and covered with a PMMA layer doped with quantum dots (QD) made of PbS. Two grating patterns (a coupling and an outcoupling grating) were created on the Au film. The probe signal coupled to the coupling grating was at a wavelength of λ_{probe}=633 nm and it created propagating SPPs at a wavelength around λ_{SPP}=1160 nm. The QD doped PMMA was pumped with a HeNe laser at λ_{pump}=633 nm and the QD emission would be coupled to the gold SPP waves. A schematic of the experimental setup is shown in Figure 12. At low pump intensity, gain in the structure could be observed. It was measured to be optimized at g=17 cm^{-1} while the propagation length of the SP waves increased by 30%. As the pump intensity would increase, the SPP-ASE would dominate but no net SPP gain was observed.

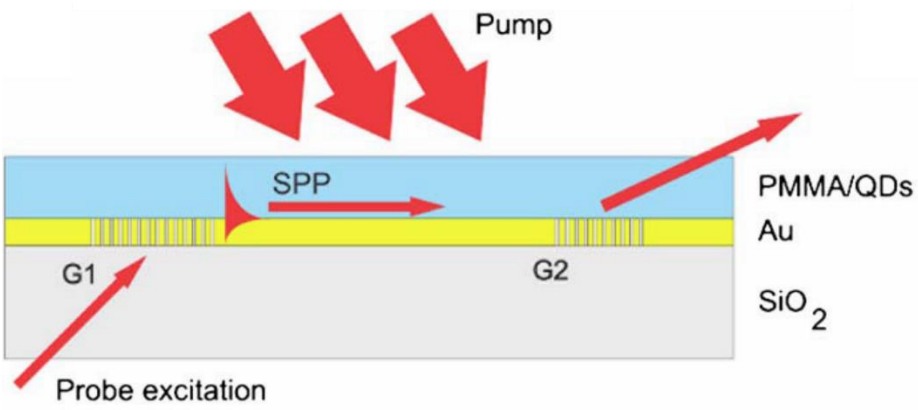

Figure 12 Experimental setup for stimulation of SPPs by QD doped excitation. G1 and G2 are the coupling and output gratings respectively. Adopted from Ref. [26], Copyright (2010), with permission from OSA.

Noginov and colleagues [27, 28] demonstrated stimulated emission into SPPs on a silver film (thickness t=39-81 nm) with an R6G doped top layer of PMMA (t=1-3 μm). The experimental setup followed the attenuated total reflection geometry. They pumped the amplifier region at a wavelength λ_{pump}=532 nm, varying the pump intensity. They observed laser-like emission of SPPs accompanied by a narrowing of the emission spectrum (characteristic of stimulated emission into SPPs) above a certain pump intensity threshold. This emission was also dependant on the angle of coupling, supporting the claim that the detected signal was stimulated SPPs.

De Leon and Berini [29] developed a theoretical model to calculate the expected gain from single interface SP modes and LRSPP modes supported by a metallic waveguide structure topped with a gain medium. The gain medium considered consisted of dye R6G in solution. De Leon and Berini latter tested the theoretical model for gain calculation experimentally [23] and they successfully observed experimentally amplification of the mode beyond loss compensation in the near-infrared, due to the use of LRSPP low attenuation properties. The fabricated and tested structure consisted of a 1 μm wide and 20 nm thick gold stripe on a SiO_2 substrate, topped with a gain medium made of IR140 dye molecules in solution. The gain medium was optically pumped by a dye laser at λ_{pump}= 808 nm and the size of the pump could be varied to

increase or decrease the amplifier length. The probe signal, at a wavelength of λ_{probe}=882 nm, was coupled via end-fire coupling from a PM fibre to the stripe waveguide end-facet. The experimental setup is shown in *Figure 13*. By comparing the output power in an I_{pump}=0 J/cm^2 situation to a pumped gain situation, they could retrieve the input to output gain as a function of the amplifier length. The LRSPP propagation losses were overcompensated by the gain in the medium, giving a mode power gain MPG=8.55 dB/mm.

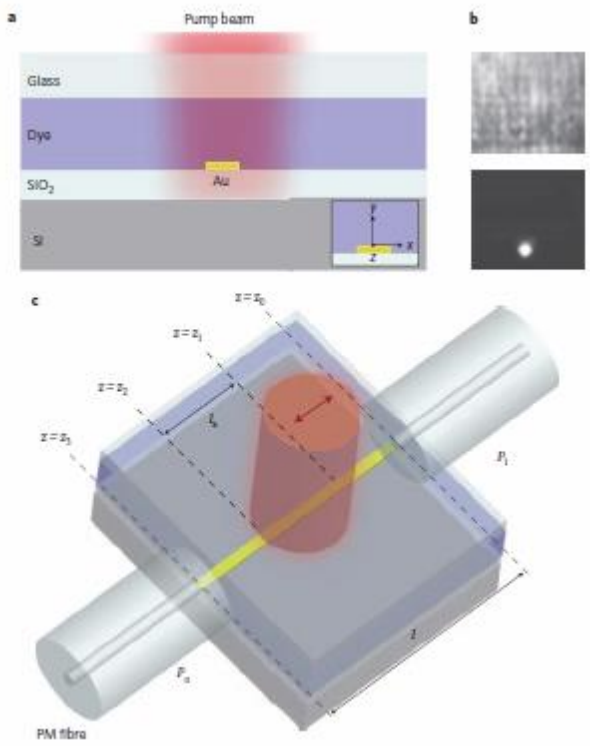

Figure 13 ***a)*** *Cross-sectional view of device under test,* ***b)*** *mode image for pump on probe off (top) and pump off probe on (bottom),* ***c)*** *schematic of the experimental setup [23] Reprinted by permission from Macmillan Publishers Ltd: [Nature Photonics] (De Leon, Israel, & Berini, Pierre (2010). Amplification of long-range surface plasmons by a dipolar gain medium. nature photonics* ***37****, 382.), copyright (2010)*

Gather and colleagues [30] presented strong evidence of amplification overcoming propagation loss in LRSPP mode in the visible spectrum. The structure tested was composed of a thin layer of gold (t=4 nm) bounded between two layers of

polymer, the top one being the gain material made of poly(spirofluorene). The gain material was pumped at λ_{pump}=532 nm using a YAG laser forming a stripe (defining the geometry of the amplifier) of width 200 μm and variable length. The emission was collected from the sample edge. A schematic of the experimental arrangement is seen in Figure 14. Narrowing of the spectrum (with a peak emission at λ=598 nm) and dramatic change of slope in the emitted intensity as a function of the pump stripe length strongly indicated ASE and the overcompensation of loss in the waveguide. Using the variable slit length method (VSL, described in a subsequent section), they measured the net gain coefficient to be g=8±2 cm^{-1}.

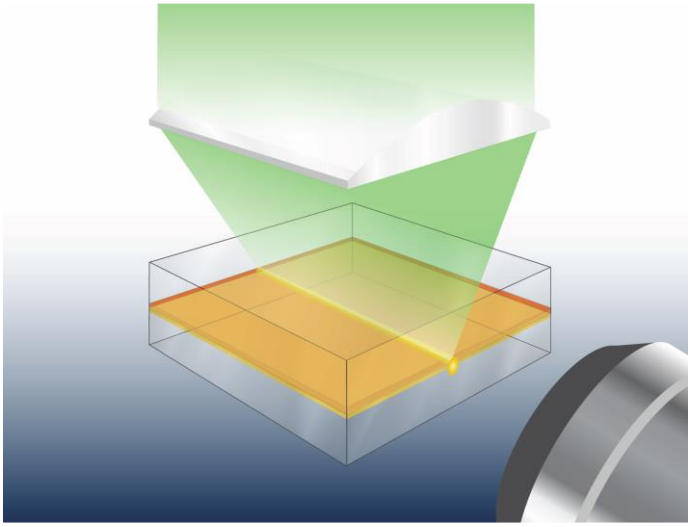

*Figure 14 Schematic of the experimental arrangement [30] Reprinted by permission from Macmillan Publishers Ltd: [Nature photonics letters] (Gather, M. C., Meerholz, K., Danz, N., & Leosson, K. (2010). Net optical gain in a plasmonic waveguide embedded in a fluorescent polymer. nature photonics Letters **4**, 457.), copyright (2010)*

Hahn and colleagues [31] studied a LRSPP waveguide bounded by two symmetric gain media. The structure fabricated and tested consisted of a thin silver film (t=25 nm) deposited on IR-140 doped PMMA (t=5 μm) and coated with a t=950 nm layer of doped PMMA, thick enough to preserve the symmetry of the claddings but thin enough to avoid significant pump absorption. Pumping was applied through the top by an optical

parametric generator (λ_{pump}=808 nm) and the waveguide was defined by the pump stripe width and length. The emitted signal was collected by an objective lens and passed through an analyser p or s oriented. The TE and TM spectra (shown in Figure 15) were acquired and it was found that the TM orientation dominates. The peak wavelength of the emitted LRSPP was λ=868 nm. The variable slit length (VSL) method was applied to measure the modal gain g_{mod}. For a double gain layer structure, the modal gain measured was g_{mod}=16.7 cm^{-1}.

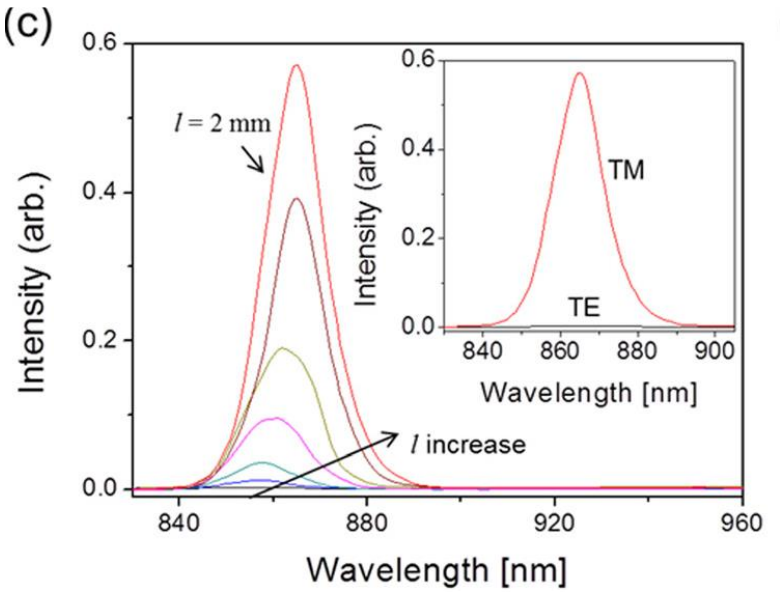

Figure 15 LRSPP-ASE intensity spectrum for different pump stripe lengths. Inset: polarisation-resolved intensity spectrum with an analyzer in the collection setup. The TE polarized spectrum is low due to the TM nature of LRSPP waves [31] © 2015, Rights managed by AIP Publishing LLC.

1.4 Toward plasmonic lasers

The perspective of creating a coherent source of SPP waves is very attractive. This laser could be integrated with biosensing devices and their utilisation would ease the data acquisition. Researchers proposed different approaches to design the laser resonator. The first known single mode SP laser based on a DFB grating design was

designed and tested by Tredicucci and colleagues [32]. The structure consisted of a metal grating (made of periodic sections of Au and sections of Ti/Au with dc=50%, thus creating a refractive index perturbation along the stripe and acting as a DFB resonator) interfaced to a semiconductor pumped via electron injection. The emitted wavelength was λ=17 μm, in the far-infrared (FIR) where the SP loss is very low due to poor absorption in the metal at these wavelengths, therefore it was easy to compensate and overcome loss for that waveguide.

Jetté and Berini [33] designed and fabricated a plasmonic laser based on an external cavity design, where a plasmon polariton Bragg grating (PPBG) supporting LRSPP modes acts as a distributed Bragg reflector (DBR) while the gain element is a InP gain chip, emitting at λ=1550 nm. The PPBG had a length L_G=5 mm, consisting of a concatenation of unit cells formed of a Au/Mo stripe, each unit cell having a section w_1=8 μm and w_2=3 μm, pitch Λ=1.6 μm (third order) and dc=50%. The Bragg reflectance was measured to be 10% at λ_B=1544.08 nm in a passive situation. The InP gain chip was connected to the Bragg waveguide using a PM-SMF on one end of the waveguide, while the other end facet was the output to the laser. Figure 16 shows a schematic of the laser configuration. The threshold diode current for lasing action was 57 mA and the maximum output power obtained was 2 mW. Figure 17 displays a lasing mode obtained from this ECL-PPBG configuration.

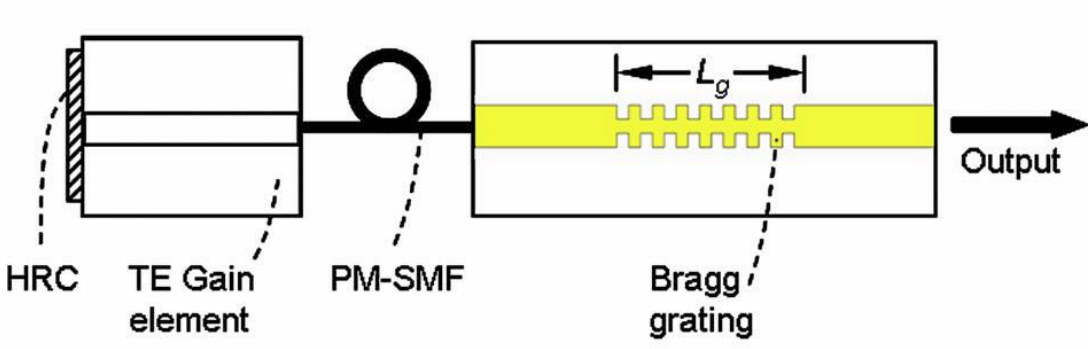

Figure 16 External cavity laser using a PPBG as a resonator [33] © 2007, Rights managed by AIP Publishing LLC.

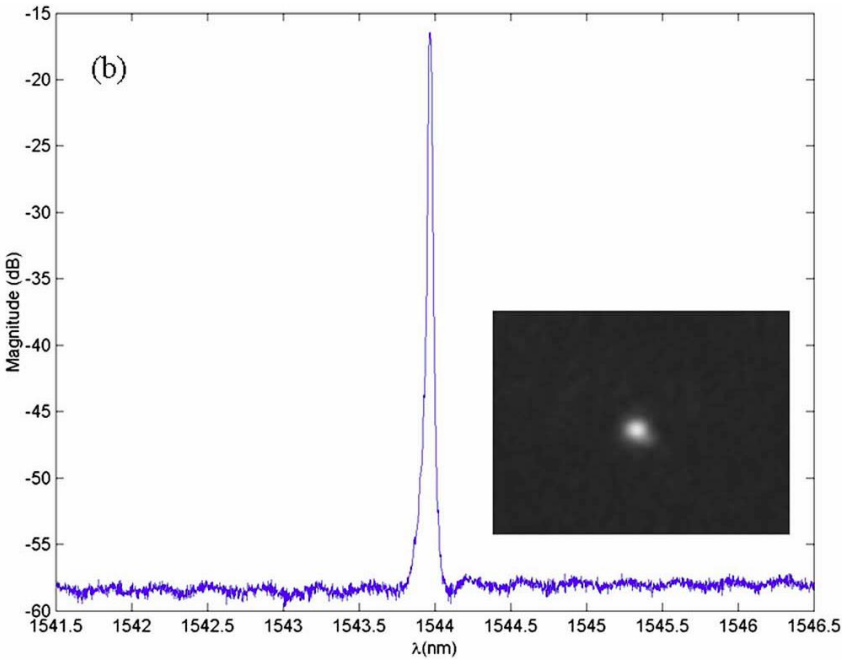

Figure 17 Output spectrum of the external cavity laser [33] © 2007, Rights managed by AIP Publishing LLC.

Oulton and colleagues [34] designed, fabricated and tested experimentally a tightly confined plasmonic laser based on a hybrid plasmonic waveguide. The design consisted of a semiconductor nanowire made of high-gain cadmium sulphide (CdS) acting as the resonant cavity (the end-facets reflect the plasmonic modes), a silver film and a thin insulating layer of magnesium fluoride in between (schematic seen on Figure

18). This laser was pumped at a wavelength λ_{pump}=405 nm and the emission collected was at a wavelength λ=489 nm. The coupling between the surface plasmon modes at the Ag film and the cavity modes in the nanowire creates a strongly confined mode due to the thin (t=5 nm) gap between them. The authors claimed to obtain a mode size as small as $\lambda^2/400$. The lasing intensity threshold was lower than for regular semiconductor CdS nanowire laser, although the lasing doesn't have a single mode, presenting a multimode cavity resonance.

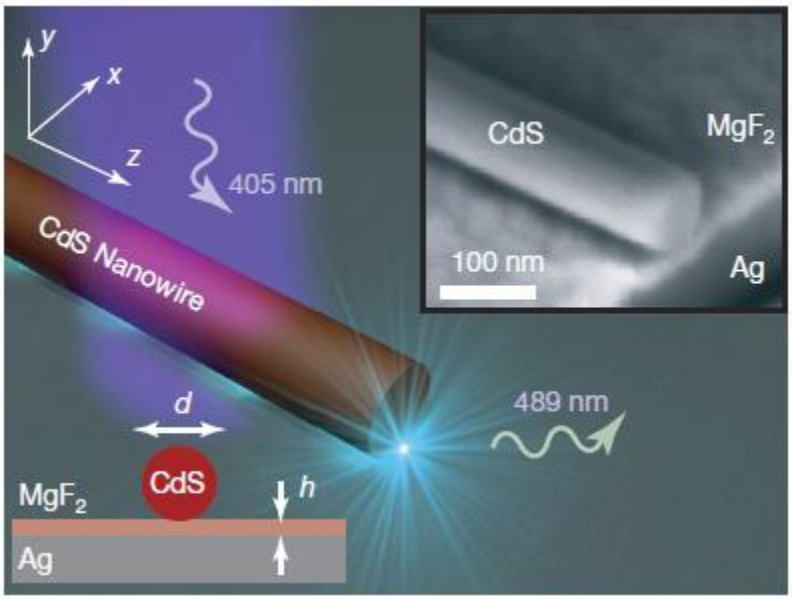

*Figure 18 Schematic of the nanowire-gap-silver film structure [34] Inset: Scanning electron microscopy (SEM) of the nanowire plasmonic laser. Reprinted by permission from Macmillan Publishers Ltd: [Nature Letters] (Oulton, R. F., Sorger, V. J., Zentgraf, T., Ma, R.-M., Gladden, C., Dai, L., . . . Zhang, X. (2009). Plasmon lasers at deep subwavelength scale. Nature Letters **461**, 629.), copyright (2009)*

Keshmarzi and colleagues [35] characterized the amplifying properties of dye molecule IR-140 in a solid film made of polymer (PMMA). The main objective was to optimize the conditions resulting in maximum material gain (g_{mat}) for subsequent use of this amplifying medium in the creation of plasmonic lasers based on PPBGs supporting LRSPPs stimulated by the doped dielectric medium. The parameters under scrutiny were

the IR-140 concentration (in molecular weight, m.w.) and the pump intensity (I_p). The signal polarisation was also verified to confirm that enough TM gain is present in the dielectric layer to amplify LRSPP modes, which are only supported in the TM polarisation [5]. The method followed to measure the g_{mod} was the variable slit length (VSL) method, where a narrow pump strip (repetition rate of 10 Hz and λ_{pump}=808 nm) illuminates the sample and the emitted spectra is collected from its edge for different stripe lengths while maintaining I_{pump} constant and the results are fitted to an equation relating the amplified spontaneous emission intensity I_{ASE} to the pump stripe length L:

$$I_{ASE} = \frac{J_{sp}}{g_{mod}}(1 - e^{g_{mod}L}) \qquad (8)$$

This equation derives from the integration from L=0 (assuming that $I_{ASE}(L=0)=0$) to L of equation 5. The modal gain g_{mod} is extracted from this equation. The optimal conditions for maximum modal gain, measured to be g_{mod}=68 cm^{-1}, were found for a IR-140 concentration of m.w.=0.8% and a pump intensity I_{pump}=43.4 mJ/cm^2.The PMMA layer was thick enough to contain most of the supported slab modes, and the confinement factor was approximately 1. The material and modal gains are thus similar. Inserting an analyser at the collection branch of the setup showed that the ASE signal is non-polarised if the pump polarisation is parallel to the stripe.

Keshmarzi and colleagues [36] proposed an original concept for a plasmonic laser based on LRSPP supported on step-in-width Bragg gratings. The structure presented is a silver stripe (w=1 µm, t=20 nm) on a passive substrate (such as passive PMMA or SCHOTT glass) with an amplifying top layer made of PMMA doped with a dye molecule (IR-140) in a molar concentration previously measured to obtain optimal material gain [35]. The gain layer should be pumped from the top and this would generate stimulated emission of LRSPP for lasing action while the PPBG would serve as

the resonator. Three plasmonic laser designs based on grating structures supporting LRSPP were investigated: the distributed Bragg reflector (DBR) and high reflection coating with DBR, both in external cavity laser (ECL) configuration and the distributed feedback (DFB) laser. The simple DBR is a silver stripe coated with doped PMMA (t=2 μm), bounded by two PPBGs (coated with passive PMMA) responsible for the oscillation, one having high reflectance while the other has lower reflectance, acting as the laser output. The active straight waveguide region and the two PPBGs define the length of the laser cavity. This laser configuration benefits from a greater tuning range. The HRC-DBR configuration is similar but one of the DBRs is replaced with a high reflection coating (HRC) to reduce the cavity length, thus increasing the mode spacing (for single mode application) although reducing the tuning range. The DFB configuration places the doped PMMA directly on top of a first order PPBG. From coupled mode theory, this structure refractive index perturbation between each section of width w_1, w_2 generates diffractions modes, but only two counterpropagating (forward and backward) modes will be amplified into lasing due to phase-synchronization. The design study included LRSPP mode analysis to obtain the effective index of the LRSPP, and derive the mode power gain (MPG) in the active region, a TMM simulation to obtain the theoretical R, T, λ_B and $\Delta\lambda_B$ of all gratings, and carefully choosing the length of each grating to respect the single mode lasing condition (that the gain obtained from the active region overcomes loss, that the phase condition is met, and that only one cavity mode overlaps with the Bragg bandwidths). Heating the waveguide via injection of electrical current is suggested as a means for thermal tuning of the lasers. The parameters affected would be the dielectric effective refractive index, modulated by the thermo-optic effect. Figure 19 shows a schematic of a proposed plasmonic LRSPP laser, based on the DFB design with a uniform periodic PPBG.

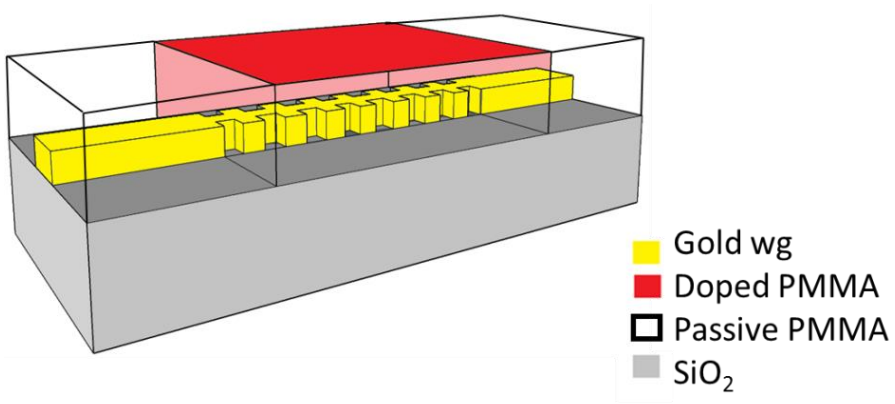

Figure 19 3D schematic of a LRSPP laser, based on a PPBG DFB plasmonic laser

1.5 Thesis objectives

This thesis contributes to the realisation of plasmonic lasers based on plasmon polariton Bragg gratings. The scope of this thesis is twofold. In the first section, entitled *Passive plasmonic Bragg grating characterization*, the results of the testing and characterization of a new design of plasmonic Bragg gratings in the near-infrared are presented. The reflectance and transmittance responses expected from plasmonic Bragg gratings (PPBGs) are obtained theoretically using the transfer matrix method (TMM) and the numerical model is validated experimentally. The experimental setup and procedures followed are described in detail. In the second section, an in-depth analysis of the gain medium (IR-140 dye doped poly(methyl methacrylate) better known as PMMA) is performed. This gain medium was selected as the top gain layer for the active plasmonic gratings and lasers designed by my colleague, Ph.D. candidate Elham Karami Keshmarzi.

The remainder of this thesis is organised as follows. The second chapter, entitled *Passive plasmonic Bragg grating characterization*, treats the investigation performed on the PPBGs, while Chapter 3, *Gain optimisation and bleaching of IR-140 doped PMMA,* is a manuscript (soon to be submitted for publication) on IR-140 doped PMMA as a gain

medium for plasmonic Bragg lasers. This thesis ends at Chapter 4, *Conclusion,* with some concluding remarks as well as prospects for future work.

Chapter 2: Characterisation of plasmon polariton Bragg gratings

In this chapter, my work on the characterisation of passive plasmon polariton Bragg gratings (PPBGs) is described. The chapter is divided into five sections, which are *Architecture and Fabrication* of PPBG structures, followed by *Numerical modelling of Bragg gratings using the Transfer Matrix Method* describing the method for the numerical modelling of PPBG performance. *Experimental setup and procedure* relays a detailed version of the experimental protocol followed while *Results and discussion* gives the data obtained from the analysis of PPBGs and provides insightful comments on the discrepancies between the results from the modelling and the experiment. The *Conclusion* section briefly summarizes the accomplishments of this thesis work.

2.1 Architecture and Fabrication

Each device consists of a series of waveguides with different widths. On a device, PPBGs with three different pitches (Λ_1, Λ_2 and Λ_3) are present, as well as a few straight waveguides (SW).

Passive PPBGs consist of a Bragg grating bounded by two sections of SW with width of 1 µm. The gold thickness remains constant (20 nm) throughout the entire waveguide. The grating sections consist of a concatenation of cells each having a length Λ defined as the pitch and 2 sections of widths w_1, w_2 and length d_1 and d_2 [17] as can be seen in Figure 20. The duty cycle (dc) determines the proportions between d_1 and d_2 and is given by:

$$dc = \frac{d_1}{\Lambda} * 100\% \qquad (9)$$

The PPBGs under study in this work had a uniform dc of 50%, which implies that d_1 and d_2 have the same length. Section 1 had a gold width w_1=1 µm while section 2 had a width w_2=0.5 µm. The gold width of a section is a determining factor in the effective refractive index of that section. Different widths have a different effective index n_{eff}, and it is this difference in refractive index that causes a perturbation in the wave, leading to grating phenomena [15]. If this perturbation is periodic, the partial reflections at each transition of sections with different n_{eff} through the grating can add constructively to form a narrowband Bragg reflection following the Bragg condition:

$$\lambda_B = \frac{2*n_{ave}*\Lambda}{O} \qquad (10)$$

where λ_B is the resonance Bragg wavelength at which the two counterpropagating (forward and backward) LRSPP modes are superposing constructively due to respect of the phase condition which stipulates that the optical path phase must be an integer multiplied by 2π. O is the order of the grating and can be an integer equal to one or higher. In the case of the structures of interest in this work, the grating order was always equal to one. n_{ave} is the average effective index of refraction between both sections, and is given by:

$$n_{ave} = \frac{n_1 d_1 + n_2 d_2}{\Lambda} \qquad (11)$$

Indices n_1 and n_2 are respectively the effective indices of the LRSPP modes supported by section 1 and section 2. These values are calculated via numerical simulation and the method is presented in *section 2.2*. The number of unit cells, determining the entire length of the gratings, remained fixed at N=6000. The grating length is thus given by:

$$L_{PPBG} = N * \Lambda \qquad (12)$$

Figure 20 shows a schematic of a PPBG, with each key parameter identified.

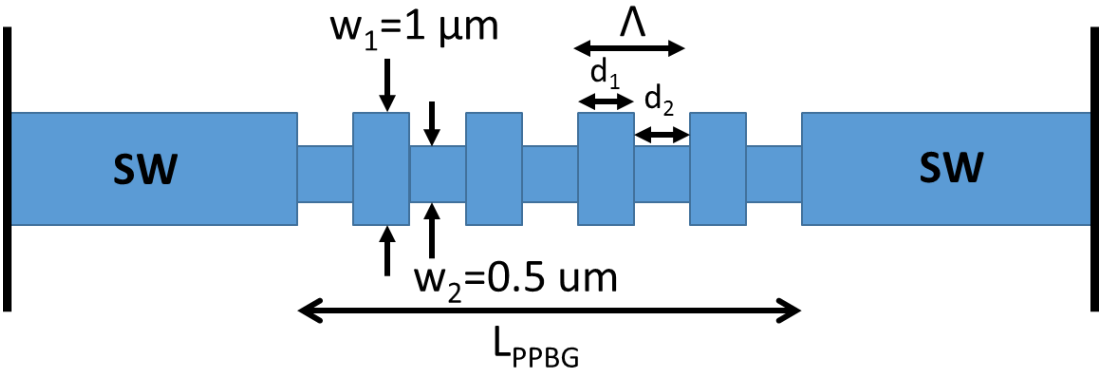

Figure 20 Schematic of a PPBG consisting of the Bragg grating bounded by two sections of SW

Three different pitches Λ were designed, each with a specific λ_B and L_{PPBG} although the dc and the number of unit cells N were kept respectively at 50% and 6000. Table 1 briefly summarizes the main characteristics of each grating design. Modelling results for these designs are presented in the next section.

Table 1 Three design specifications for PPBG

Design	Pitch (Λ)	Length L_{PPBG}	λ_B
	[nm]	[µm]	[nm]
1	293	1758	851.40
2	303	1818	880.46
3	313	1878	909.52

The length of the SW segments varies slightly from one device to the other, since it depends on the cleaving position. Cleaving marks were added to the layout of the structures, and the SWs were elongated on both sides of each structure to ensure a continuous waveguide from one end facet to the end. As an example, the lengths from the two devices giving promising results (that will be presented in the *Results and discussion* section) are respectively $L_{device\ 1}$=2.54 mm and $L_{device\ 2}$=2.29 mm. To obtain the length of each SW segment, one can do this simple calculation:

$$L_{SW} = \frac{L_{device} - N*\Lambda}{2} \qquad (13)$$

which is specific to each grating pitch. The SW segment lengths of the PPBG presented in the *Results and discussion* section are respectively L_{SW1}= 291 µm and L_{SW2}= 236 µm.

The fabrication of Bragg gratings was performed by my colleague, PhD candidate Elham Karami Keshmarzi. Electron beam lithography is applied to a silica (SiO_2) wafer with thickness 15 µm grown on a silicon (Si) substrate of thickness 500 µm, coated by a resist of Poly(methyl methacrylate) (PMMA) to define the different gratings. The wafer is developed to remove the PMMA that received the waveguide designs. A 20 nm thin film of gold is then evaporated and PMMA is gently removed by lift-off using Acetone. The thickness and quality of the metallic waveguide structures are analyzed using scanning electron microscopy (SEM) and atomic force microscopy (AFM) techniques. A 600 nm thickness of PMMA is spin-coated on the whole surface of the wafer. The wafer is then cleaved carefully into devices ready to be tested. The silicon substrate facilitates the cleaving process and the facets obtained are of good optical quality.

2.2 Numerical modelling of Bragg gratings using the Transfer Matrix Method

SPP modes are supported at the interface of two media with opposite real dielectric constant. Structures composed of a metal (with negative real dielectric constant) of finite width and small thickness embedded in a weakly asymmetric configuration ($n_1 \approx n_3$) between two media with positive (but not equal) real dielectric constant can support LRSPP modes [4]. PPBGs under test in this study follow this weakly asymmetric structure design, as they are made of a thin gold stripe with thickness t_{Au}=20 nm and finite width w_{Au1}=1 μm and w_{Au2}=0.5 μm on a SiO_2 substrate with thickness t_{SiO2}=15 μm and covered by a PMMA layer with thickness t_{PMMA}=600 nm. The complex refractive index of each material, taken from [37] at a wavelength λ=880 nm, is $\tilde{n}_{Au}$ = 0.22139 – i 5.3141, $\tilde{n}_{SiO2}$ = 1.452 and $\tilde{n}_{PMMA}$ = 1.4835. The complex refractive index of a material is related to its complex dielectric constant as:

$$\tilde{n}^2 = \tilde{\varepsilon} \qquad (14)$$

Figure 21 shows a cross section of the waveguide with each key parameter identified.

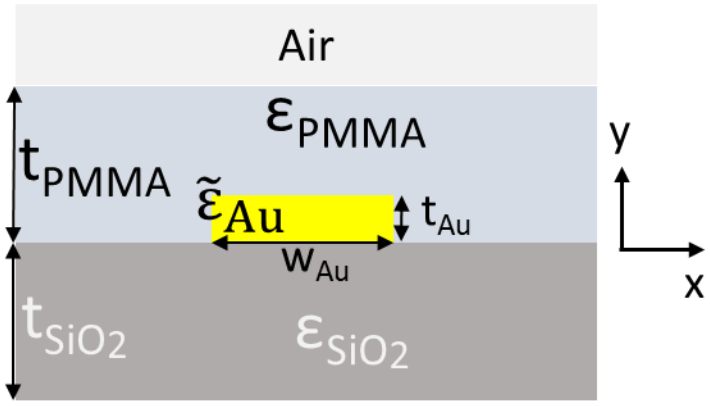

Figure 21 Cross section of the waveguide structure used for PPBG

The effective refractive index of the mode propagating in this waveguide section is needed to evaluate the Bragg grating performance, since it is the difference in effective index that induces the perturbation causing the reflected wave at the interfaces between sections. The effective refractive index $\tilde{n}_1$ of the mode propagating in a section of width w_1 as well as $\tilde{n}_2$ for w_2 must be calculated numerically, using software (Comsol) that will solve the electric and magnetic vector wave equations with boundary conditions using the finite element method (FEM) for a specific geometry and material parameters. The electric field propagating in the out-of-plane axis (z-axis in Figure 21) can be expressed as:

$$\tilde{E}(\vec{r},t) = E(x,y)e^{i\omega t - kz} \qquad (15)$$

with the wavenumber k, having real (α, attenuation constant) and imaginary (β, phase constant) parts being specific to the waveguide supporting the wave. Following the condition of continuity for the electrical and magnetic fields at the interfaces between the gold film and the claddings (at y=0 and y=t_{Au} on Figure 21 for the E_x component, and x=±w_{Au}/2 for the H_y component) lead to an expression for the allowed propagation constant in the structure from which the effective refractive index is extracted. This allowed propagation constant is found by solving an eigenvalue problem of the form:

$$\vec{\nabla} \times \mu^{-1}\vec{\nabla} \times \vec{E}(\vec{r},t) - \lambda\vec{E}(\vec{r},t) = 0 \qquad (16)$$

where E(r,t) is the real part of equation 15 while λ is the eigenvalue to be calculated, written as:

$$\lambda = k_0^2(\varepsilon_r - i\sigma/\omega) \qquad (17)$$

where k_0, ε_r, σ and ω are respectively the free space wavenumber, the relative permittivity, the conductivity and the angular frequency.

The obtained results of interest are the effective mode index and the electric field cross section profile, as shown in Figure 22.

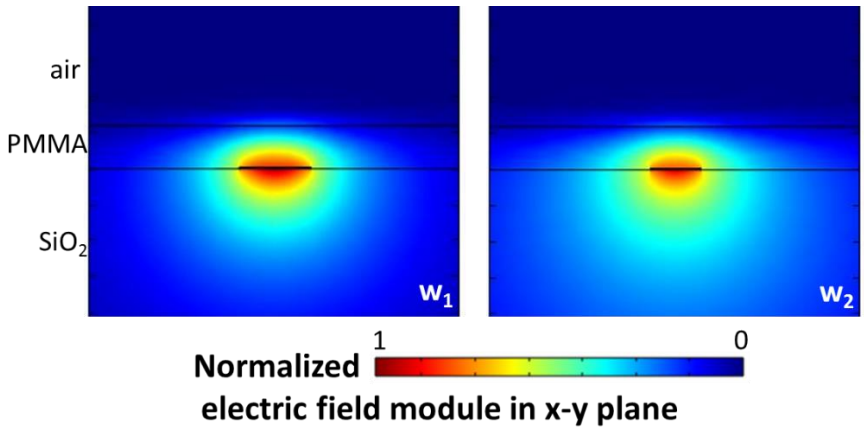

Figure 22 Normalized electric field profile of a cross sectional area of the waveguide, for w_1 and w_2 obtained from Comsol FEM simulation. Calculated effective mode indices are respectively $\tilde{n}_1=1.4536-i1.0337*10^{-4}$ and $\tilde{n}_2=1.4522-i3.5496*10^{-5}$

The sections 1 and 2 therefore have different effective refractive indices, $\tilde{n}_1=1.4536-i1.0337*10^{-4}$ and $\tilde{n}_2=1.4522-i3.5496*10^{-5}$ which lead to a perturbation in the wave at the interface between sections 1 and 2. This change in effective index will lead to a nonzero reflectance of the wave at the interface.

The objective for Bragg characterization is to obtain the reflectance and transmittance of the LRSPP mode through the entire grating. To analyze the electric fields changes between medium 1 and 2, one can use the Maxwell equations. Figure 23 shows a schematic of the fields at the interface between medium 1 and 2. The wave propagates in the z direction. The method used, TMM, is intended for a dielectric stack but it is used in this case specifically for a TM-polarised wave incident on a stack of waveguide sections such as those described in Figure 22. The rationale for using this method is its simplicity and ease of use.

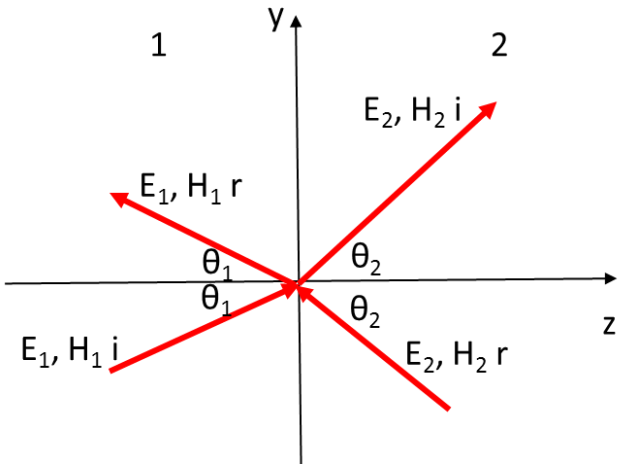

Figure 23 Fields at the interface between sections 1 and 2. Indices i and r stand for incident (right propagating waves) and reflected (left propagating waves).

The electric and magnetic field vectors E and H in each medium 1 and 2 are the superposition of the incident and reflected waves [14] and can be written as:

$$\tilde{E}_1 = (E_{1i}e^{-ik_1 \cdot r} + E_{1r}e^{ik_{1r} \cdot r})e^{i\omega t} \qquad (18)$$

$$\tilde{E}_2 = (E_{2i}e^{-ik_2 \cdot r} + E_{2r}e^{ik_{2r} \cdot r})e^{i\omega t} \qquad (19)$$

where the i and r indices stand for incident (right propagating waves) and reflected (left propagatin waves) and k_i is the complex propagation constant of each medium given by:

$$k_i = \frac{\tilde{n}_i \omega \cos\theta_i}{c} \qquad (20)$$

and the magnetic field, from Maxwell equations, can be written as:

$$H_i = \frac{i}{\omega\mu}\vec{\nabla} \times \overrightarrow{E_i} \qquad (21)$$

The modes of interest are transverse magnetic (TM) in nature. The only nonzero field components are E_y, H_x and E_z [5]. To obtain the relation between these fields over sections 1 and 2, one can use the boundary conditions at the interface for z=0, which states that:

$$E_{1y}^{\parallel} = E_{2y}^{\parallel} \tag{22}$$

$$(E_{1i} + E_{1r})\cos\theta_1 = (E_{2i} + E_{2r})\cos\theta_2 \tag{23}$$

for the electric fields parallel to the plane of the interface. For the magnetic field parallel to the interface plane (assuming a zero surface current density at the interface) the continuity gives:

$$H_{1x}^{\parallel} = H_{2x}^{\parallel} \tag{24}$$

From equation 21 and Maxwell's equations, equation 22 can be rewritten as:

$$\tilde{n}_1(E_{1i} - E_{1r}) = \tilde{n}_2(E_{2i} - E_{2r}) \tag{25}$$

These equations given by the boundary conditions can be reorganized into electric field vectors multiplied by a transmission matrix at the interfaces:

$$D_1 \begin{bmatrix} E_{1i} \\ E_{1r} \end{bmatrix} = D_2 \begin{bmatrix} E_{2i} \\ E_{2r} \end{bmatrix} \tag{26}$$

where D_i is the transmission matrix for a medium *i* and is defined as:

$$D_i = \begin{bmatrix} \cos\theta_i & \cos\theta_i \\ \tilde{n}_i & -\tilde{n}_i \end{bmatrix} \quad (27)$$

Multiplying both sides by the inverse of matrix D_1, one can rewrite equation 26 as:

$$\begin{bmatrix} E_{1i} \\ E_{1r} \end{bmatrix} = D_1^{-1} D_2 \begin{bmatrix} E_{2i} \\ E_{2r} \end{bmatrix} = M \begin{bmatrix} E_{2i} \\ E_{2r} \end{bmatrix} = \begin{bmatrix} M_{11} & M_{12} \\ M_{21} & M_{22} \end{bmatrix} \begin{bmatrix} E_{2i} \\ E_{2r} \end{bmatrix} \quad (28)$$

The reflection coefficient *r* and transmission coefficient *t* of the wave (assuming that $E_{2r}=0$) are therefore given by elements of the matrix M:

$$r = \frac{E_{1r}}{E_{1i}} = \frac{M_{21}}{M_{11}} \quad (29)$$

and

$$t = \frac{E_{2i}}{E_{1i}} = \frac{1}{M_{11}} \quad (30)$$

while the reflectance *R* and transmittance T linked to the intensities and the Poynting vector are:

$$R = \left|\frac{M_{21}}{M_{11}}\right|^2 \; and \; T = \left|\frac{1}{M_{11}}\right|^2 \quad (31)$$

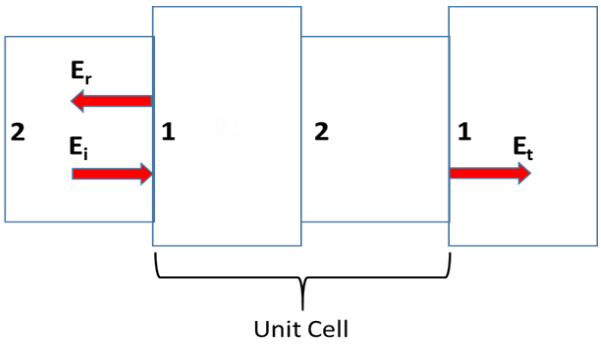

Figure 24 Incident (i), reflected (r) and transmitted (t) waves through a unit cell

Extending this method to calculate both the transmission and the reflection coefficients of the wave through a complete unit cell (see Figure 24) one gets, relating the electric fields on the left of section 1 to those on the right of section 2:

$$\begin{bmatrix} E_i \\ E_r \end{bmatrix} = D_1 P_1 D_1^{-1} D_2 P_2 D_2^{-1} \begin{bmatrix} E_t \\ E_{r\prime} \end{bmatrix} = M \begin{bmatrix} E_t \\ E_{r\prime} \end{bmatrix} \quad (32)$$

where P_i is the propagation matrix through medium *i* and is given by:

$$P_i = \begin{bmatrix} e^{ik_i d_i} & 0 \\ 0 & e^{-ik_i d_i} \end{bmatrix} \quad (33)$$

and M is the transmission matrix through the entire unit cell. The M matrix elements give the reflectance R and transmittance T of the unit cell assuming no source comes from the right ($E_{r'}$=0). In the case of a periodic Bragg grating containing N identical unit cells, the total transmission matrix M_t relates the electric fields as:

$$\begin{bmatrix} E_i \\ E_r \end{bmatrix} = M^N \begin{bmatrix} E_t \\ E_{r\prime} \end{bmatrix} = M_t \begin{bmatrix} E_t \\ E_{r\prime} \end{bmatrix} \quad (34)$$

For the specific case of the structures studied in this thesis work, the PPBG was bounded between two SW with $D_{SW}=D_1$. The input and output medium was air (n_{air}=1). The transfer matrix equation relating the electric field at the input of the waveguide to the electric field at the output is thus given by:

$$\begin{bmatrix} E_i \\ E_r \end{bmatrix}_{in} = D_{air}^{-1} D_1 P_{SW} D_1^{-1} (D_1 P_1 D_1^{-1} D_2 P_2 D_2^{-1})^N D_1 P_{SW} D_1^{-1} D_{air} \begin{bmatrix} E_t \\ E_{r\prime} \end{bmatrix}_{out} = M_t \begin{bmatrix} E_t \\ E_{r\prime} \end{bmatrix}_{out} \quad (35)$$

where D_{air} is the transmission matrix of air, defined as:

$$D_{air} = \begin{bmatrix} \cos\theta & \cos\theta \\ 1 & -1 \end{bmatrix} \quad (36)$$

and P_{SW} is the propagation matrix through the SW segments, defined as:

$$P_{SW} = \begin{bmatrix} e^{ik_1 L_{SW}} & 0 \\ 0 & e^{-ik_1 L_{SW}} \end{bmatrix} \quad (37)$$

The matrix elements of M_t give the reflection and transmission coefficients of the waveguide as stated in equation 31. This method is known as the Transfer Matrix Method (TMM) and it was used to obtain the transmission and reflection curves (as a function of wavelength) for three PPBG designs with different pitches: Λ_1=293 nm, Λ_2=303 nm and Λ_3=313 nm and a number of unit cell N = 6000 for all three designs. Figure 25 through Figure 30 give the results from this TMM study for these three designs. The angle of incidence was taken to be at normal incidence in each case ($\cos\theta_i$=1) and the effective refractive index used for each section were those calculated via FEM in Comsol, given previously. The SW segment lengths were taken as 300 µm in all three cases.

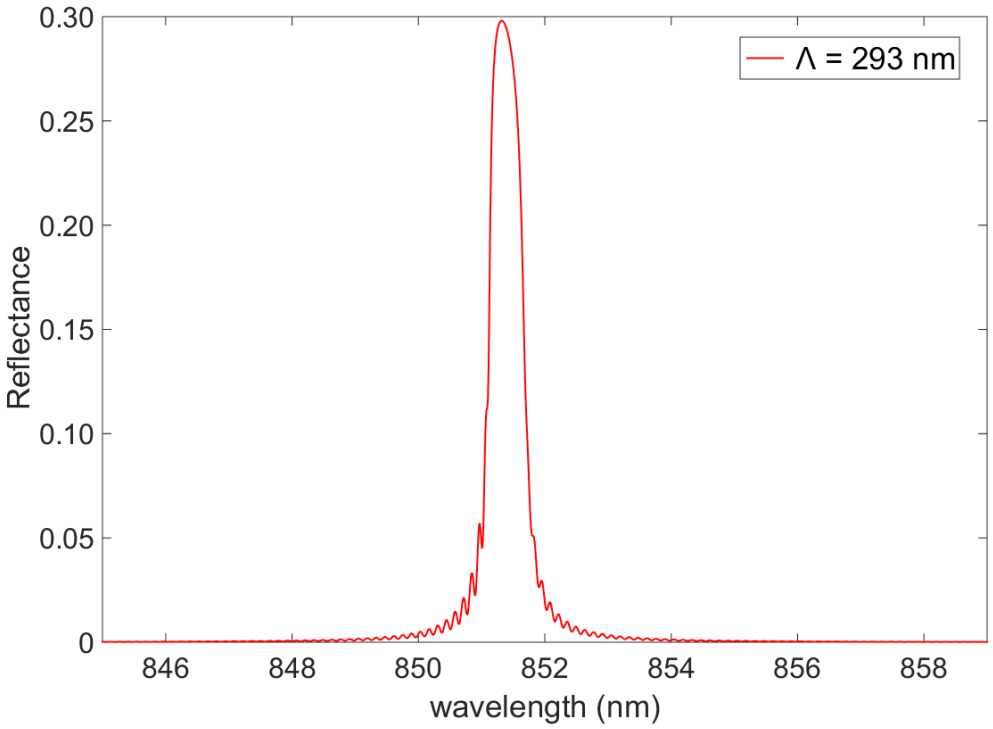

Figure 25 Reflectance of PPBG for Λ = 293 nm, N = 6000, L_{SW} = 300 µm. λ_B=851.6 nm, FWHM=0.6 nm and R=0.2977

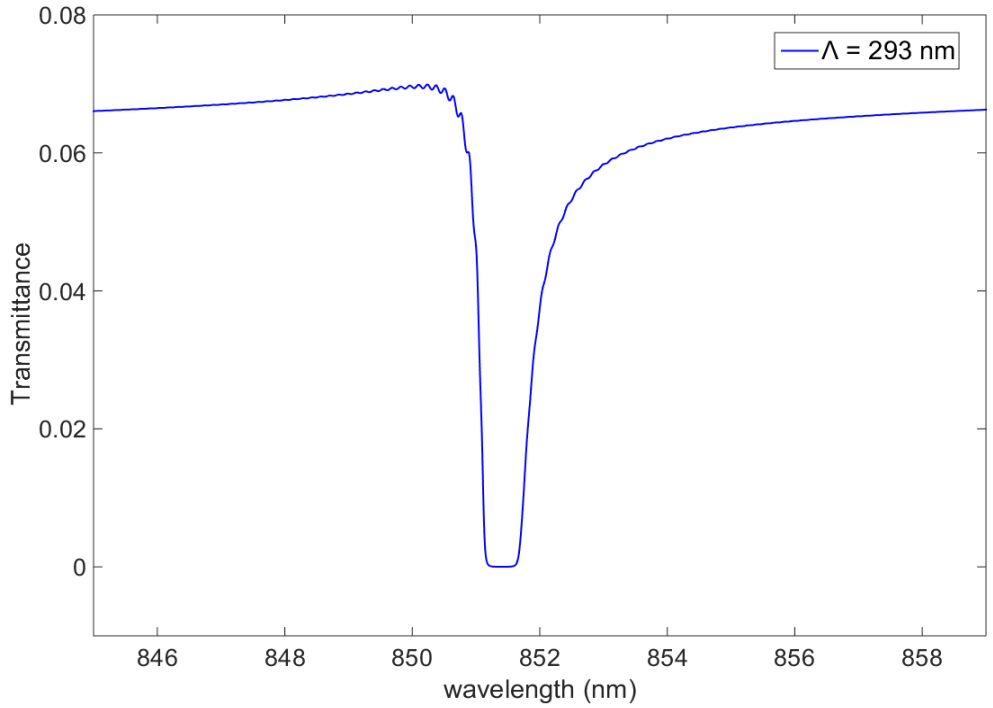

Figure 26 Transmittance of PPBG for Λ=293 nm, N=6000, L_{SW}=300 µm. λ_B=851.6 nm and FWHM=1 nm

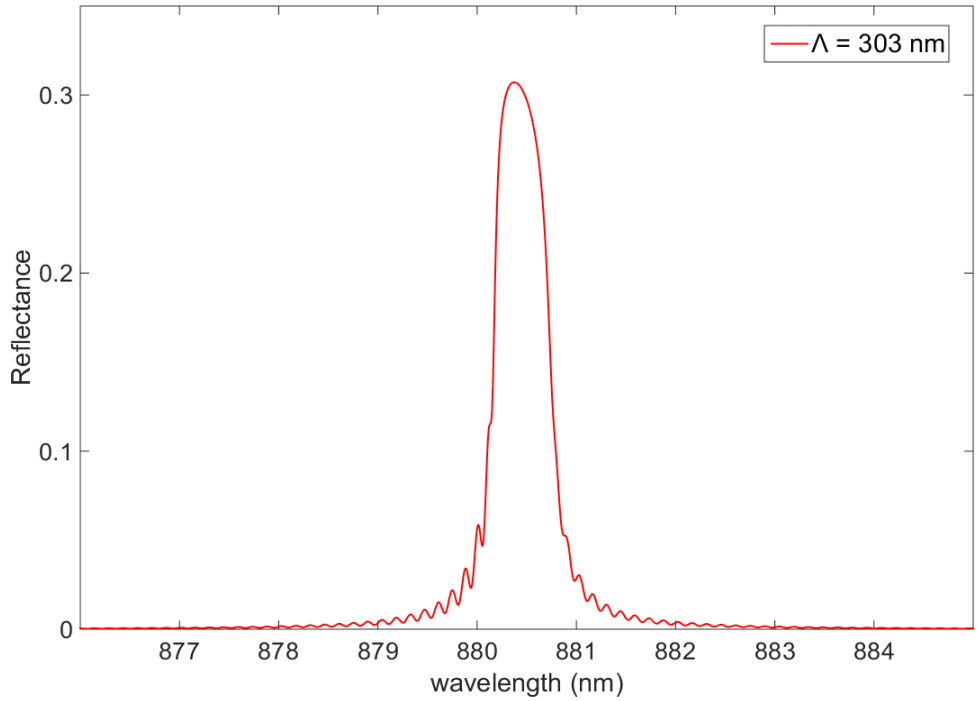

Figure 27 Reflectance of PPBG for Λ = 303 nm, N = 6000, L_{SW} = 300 µm. λ_B=880.4 nm, FWHM=0.5 nm and R=0.3072

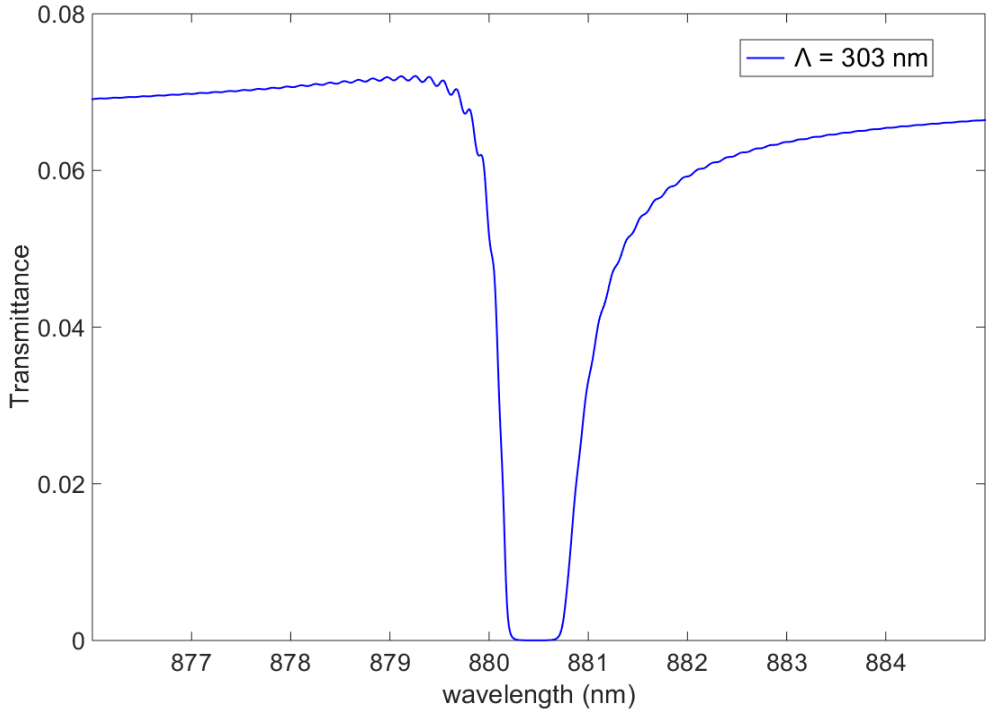

Figure 28 Transmittance of PPBG for Λ = 303 nm, N = 6000, L_{SW} = 300 µm. λ_B=880.4 nm and FWHM=0.9 nm

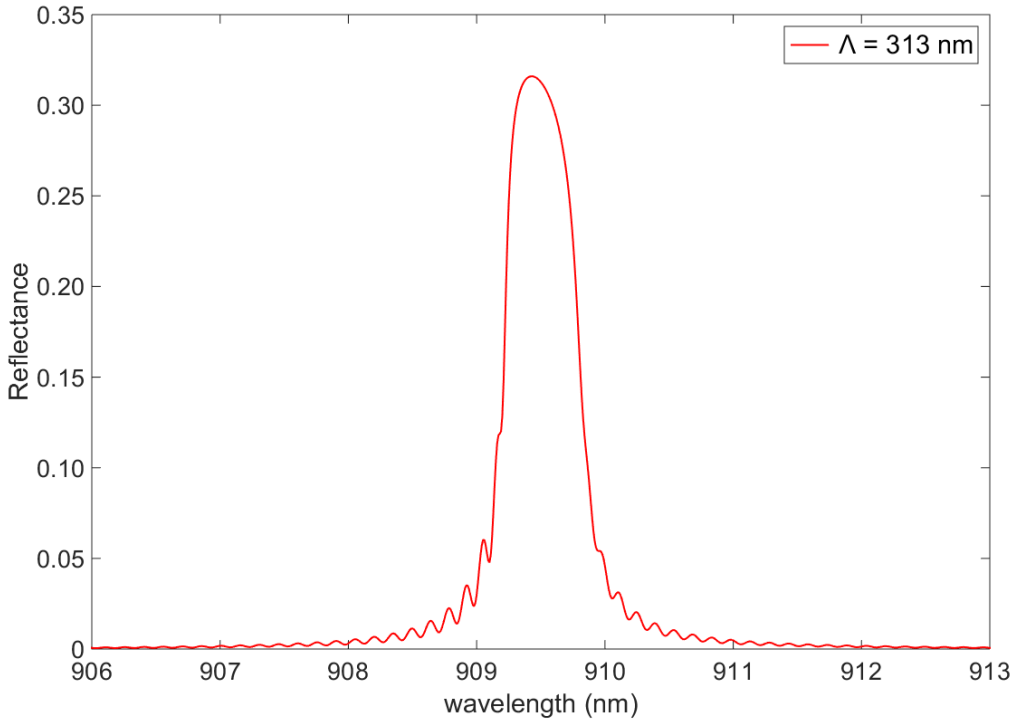

Figure 29 Reflectance of PPBG for Λ = 313 nm, N = 6000, L_{SW} = 300 µm. λ_B=909.5 nm, FWHM=0.6 nm and R=0.316

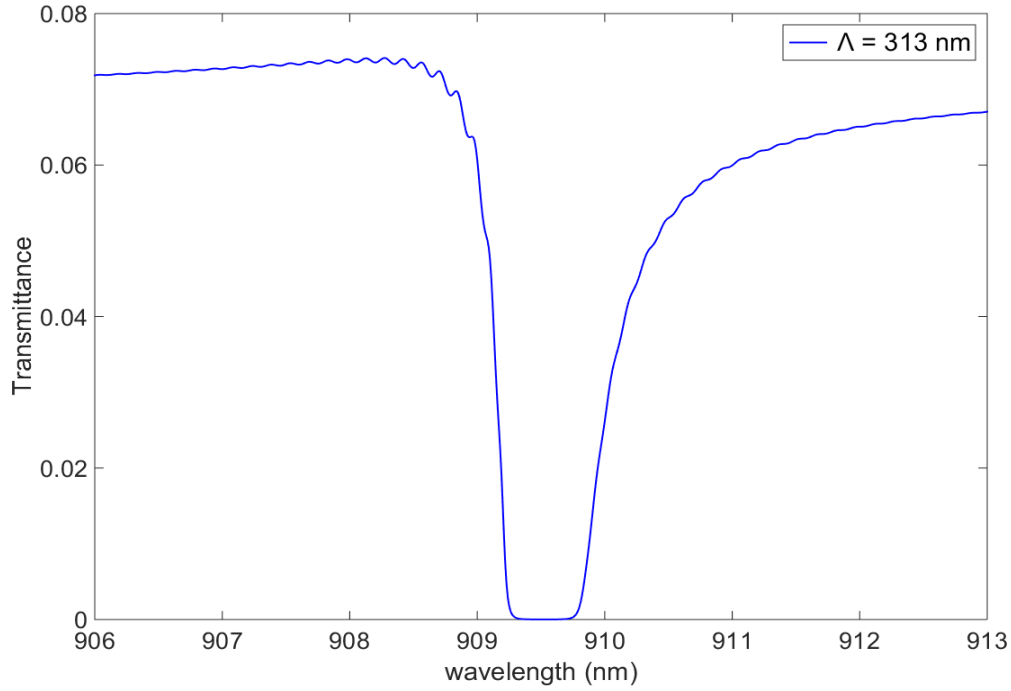

Figure 30 Transmittance of PPBG for Λ = 313 nm, N = 6000, L_{SW} = 300 µm. λ_B=909.5 nm and FWHM=1 nm

2.3 Experimental setup and Procedure

The probe laser is a CW Ti:Sapphire laser, model 3900S from Spectra-Physics (Ti:Sapph), pumped by a Centennia TD Diode-Pumped CW visible laser (pump laser). The Ti:Sapph emission wavelength can be tuned from 730 nm to 960 nm. A motorized tuner controlled via computer (LabVIEW) replaced the mechanical actuator of origin. The beam is directed to the characterisation setup via a beam splitter (BS1), mirrors (M1, M2) and BS2, as shown in Figure 31. The transmission branch through BS2 serves to monitor the probe power using a power sensor (PD1) (Newport, model 818P-001-12) while the reflection branch from BS2 corresponds to the probe beam for the system. The beam emitted by the Ti:Sapph laser is horizontally polarized, but a periscope (M1, M2) used to elevate the beam switches the linear polarisation of the beam to an arbitrary orientation. The beam is then vertically polarised using a half wave plate (WP) since LRSPP waves are TM (vertically oriented electric field) in nature.

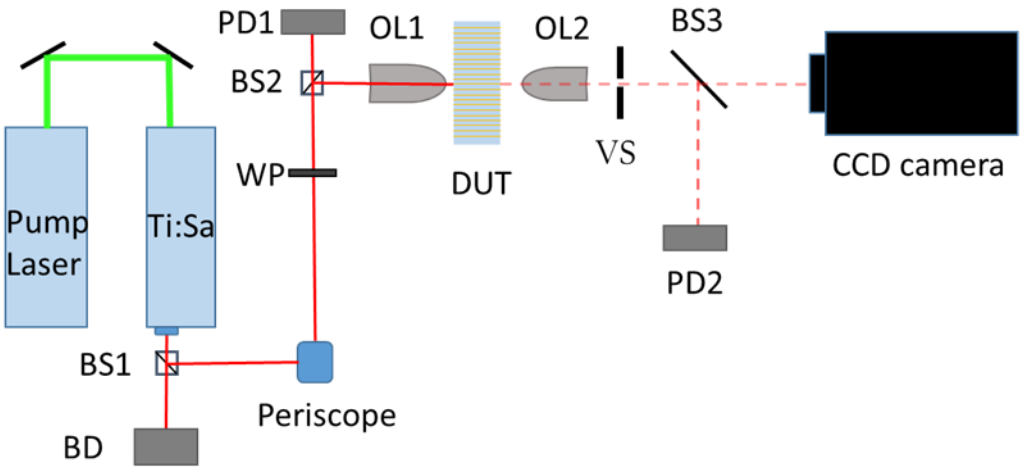

Figure 31 PPBG characterization setup. Solid path: probe beam; broken path: LRSPP mode output. Ti:Sa: Ti:Sapphire laser for probing; BSi: beam splitter; BD: beam dump; WP: wave plate; PD: power detector; OL: objective lens; DUT: device under test; VS: variable slit

The technique employed to couple the signal into the waveguide is called end-fire coupling. A 100X objective lens (OL1) was preferred to the traditional simple cleaved fibre because the size of the beam diameter that could be expected at the waist from Gaussian optics theory was closer to the LRSPP mode diameter (2 µm) while the mode field diameter (MFD) expected from a cleaved fibre was around 6 µm, causing a low coupling factor and significant background light that would superimpose on the LRSPP mode. Using tapered fibre was also explored, but this option was discarded due to the difficulties of implementing a reliable and repeatable fabrication process for tapered fibre tips. The 100X objective lens option was therefore chosen. To accurately measure the beam waist diameter w_0 and position relative to OL1, a beam profiler (BeamScan, model XYGET/LL/PWR/5Hz) was used. The resolution limit for this beam profiler is 20 µm, a beam diameter smaller than 20 µm giving inaccurate beam size results. Therefore, the beam profiler could be used directly for measuring the beam waist position relative to OL1, but could not be trusted for the waist diameter. The method used to calculate the beam waist diameter follows the Gaussian beam equations. The beam profiler was positioned at the beam waist, defined as z=0. The beam profiler was then shifted by a known displacement z_1 as can be seen in Figure 32 and the beam diameter w_1 (well above resolution limit) noted. These steps were repeated for z_2 and w_2. From Gaussian beam theory, the beam diameter is given by [22]:

$$w = w_0\sqrt{1 + {z^2}/{z_0^2}} \qquad (38)$$

where z_0 is the Rayleigh range. It represents the distance from the waist at which the beam diameter is:

$$w(z_0) = w_0\sqrt{2} \quad (39)$$

$$z_0 = \frac{\pi w_0^2}{\lambda} \quad (40)$$

With two sets of measurements of beam diameter for a distance z to the waist, one can obtain from equations 38 and 40 the beam waist diameter w_0:

$$w_0 = \frac{\lambda}{\pi}\sqrt{\frac{z_2^2 - z_1^2}{w_2^2 - w_1^2}} \quad (41)$$

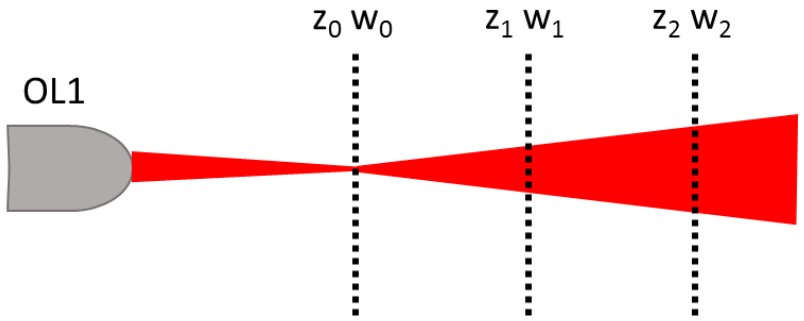

Figure 32 Approximate drawing of the probe beam path at the output of OL1.

The waist diameter calculated this way (at λ_{probe}=880 nm) was 1.32 µm, matching the size of the LRSPP mode. The distance from OL1 to the waist was measured to be 1.162 mm. The 100X objective lens was therefore adopted as the way to end fire couple the signal to the waveguide, since it is the option offering the most promising mode size matching.

Prior to adding a device under test (DUT) to the setup, a 20X microscope objective lens (OL2) was added to collect the output mode which is then directed to a beam splitter (BS3) toward an industrial color CCD camera (from Panasonic, model GP-KR222) for mode visualisation, and toward a power sensor PD2 (Newport, model 918-SL) in its reflection branch, to monitor the transmitted power. It is worth mentioning

that BS2, OL1 and OL2 are part of a cage and rod system, facilitating the alignment and focusing. Throughout the experiment, OL1 was maintained fixed while OL2 was allowed to move to focus the signal coming from either OL1 or the DUT into the CCD camera and PD2.

Before introducing a DUT into the setup, die were carefully inspected under a microscope to eliminate for test purposes structures showing a defect(s), such as gold gaps (due to liftoff problems during fabrication) or islandisation of the waveguide surface, characterized by a certain fragmentation in the gold deposition. The only waveguides tested were those presenting no visible fabrication defects. Smaller defects of fabrication such as non-periodic section lengths or over/under exposure leading to non-ideal grating shapes can only be observed through SEM or AFM. Gratings showing these defects could therefore not be detected and eliminated from the sample tests. After inspection, a DUT was added to the system, between OL1 and OL2. It was mounted on a 5-axis positioner with micrometer precision. The DUT edge was aligned parallel to the surface of OL1 and placed at the distance measured for the beam waist position, 1.162 mm from OL1. The probe wavelength was tuned to a visible wavelength (λ_{probe}<760 nm) and the focused spot was aligned to a SW or a PPBG. The probe wavelength was then tuned to wavelengths in the near infrared (λ_{probe}>850 nm) for the remaining steps of the alignment procedure because LRSPP modes propagate with lower attenuation at longer wavelengths. During the alignment procedure, the image of the output mode was inspected on a CCD camera. In a misaligned situation, a fine line is observed, representing the light transmitted through the slab waveguide consisting of the PMMA layer on the SiO_2 layer. Alignments were then performed using the multiple axes on the DUT mount until a LRSPP mode output could be visualised. It is identified by its round shape, its great sensitivity to horizontal, vertical and angular alignment and its high intensity compared to background light from the slab PMMA waveguide. Fine alignments were performed to reduce to a minimum the scattered light transmitted through the cladding, although it was not possible to completely eliminate it. Therefore, a variable slit (VS) made of two micrometer-controlled movable blades was added

between OL2 and BS3 but this addition induces some loss into the measured transmitted signal that must be taken into account in the transmission measurements.

Once the LRSPP mode emission was optimized and the background light was reduced to a minimum, a wavelength sweep was performed while monitoring PD1 and PD2. The sweep range was chosen depending on the PPBG pitch, predicting the theoretical Bragg wavelength (λ_B) at which the transmission is at minimum. The sweep steps were 0.1 nm.

PPBG designs of three different pitches were tested throughout these experiments, Λ_1= 293 nm, Λ_2= 303 nm and Λ_3= 313 nm. Λ_3 was tested on multiple waveguides but no structure showed the characteristic dip in output power indicating maximum reflection at the λ_B. Therefore, no results on design 3 are presented in the *Results and Discussion* section of this thesis work. While most of the waveguide structures for Λ_1 and Λ_2 seemed to be faulty (no dip in transmission could be registered at any wavelength) some structures did appear to function and the data acquired from these structures are shown in the section *Results and Discussion*.

The LRSPP mode output power as a function of the probe wavelength was obtained for Bragg characterization. To obtain these curves, some reference measurements and simple equations are needed to remove the effects of the setup. Each component in the setup induces loss. The effect of these losses in the system without the DUT or the VS is captured by:

$$P_{PD2} = AP_{PD1} \qquad (42)$$

where P_{PD1} and P_{PD2} are respectively the power measured at PD1 and PD2 in the absence of DUT in the setup, and A is a coefficient representing the total loss in the system. The

measured power at PD1, used to monitor the probe power incident onto the DUT end facet, is the transmitted power through BS2. The reflected power from BS2 is given by:

$$P_{probe} = BP_{PD1} \tag{43}$$

where B is a coefficient representing the ratio of reflection to transmission (the reflection is the power probing the device, P_{probe} while the transmission is the power measured at PD1) from the beam splitter BS2. The LRSPP mode power monitored on PD2, where the DUT has been added and carefully aligned to optimize the mode signal, and the VS is used for background light subtraction, is related to the incident probe power by:

$$P_{PD2-PPBG} = ALTP_{probe} \tag{44}$$

where A is the loss coefficient from all components, L is a loss coefficient comprising the loss from the coupling factor into DUT (due to mode size mismatch) and the loss from the VS, T is the transmittance through the DUT including the Bragg grating, $P_{PD2\text{-}PPBG}$ and P_{probe} are respectively the measured output power from the PPBG and the incident probe power. After some algebraic manipulations, we get the transmittance:

$$T = \left(\frac{1}{L}\right)\left(\frac{PD1}{PD2}\right)_{setup}\left(\frac{PD2}{PD1}\right)_{PPBG} \tag{45}$$

where the loss coefficient L including the coupling factor and the loss caused by VS cannot be measured experimentally, and therefore will be estimated from the simulated transmission curve for each PPBG pitch.

2.4 Results and Discussion

Figure 33 and Figure 34 plot the results obtained from designs 1 and 2 for the transmittance as a function of the wavelength, compared to the transmittance predicted by numerical simulation.

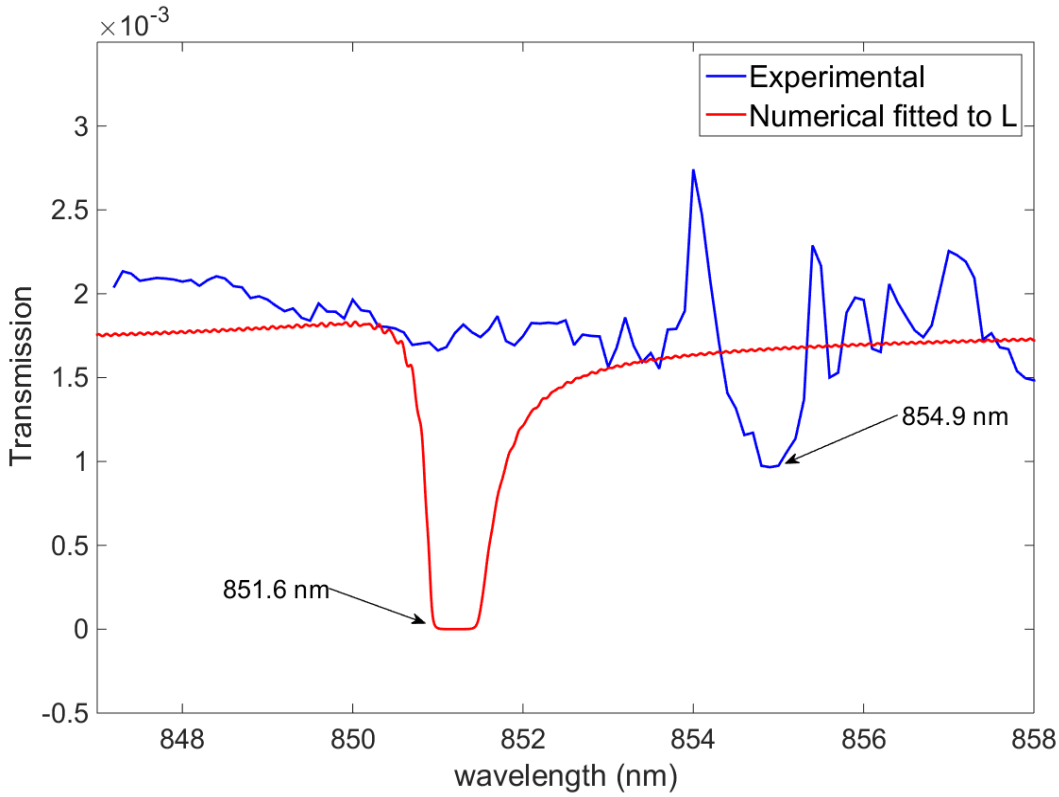

Figure 33 Experimental transmittance compared to the numerical transmittance obtained from TMM and fitted to the estimated L coefficient for a pitch Λ_1= 293 nm, measured to be L=0.3.

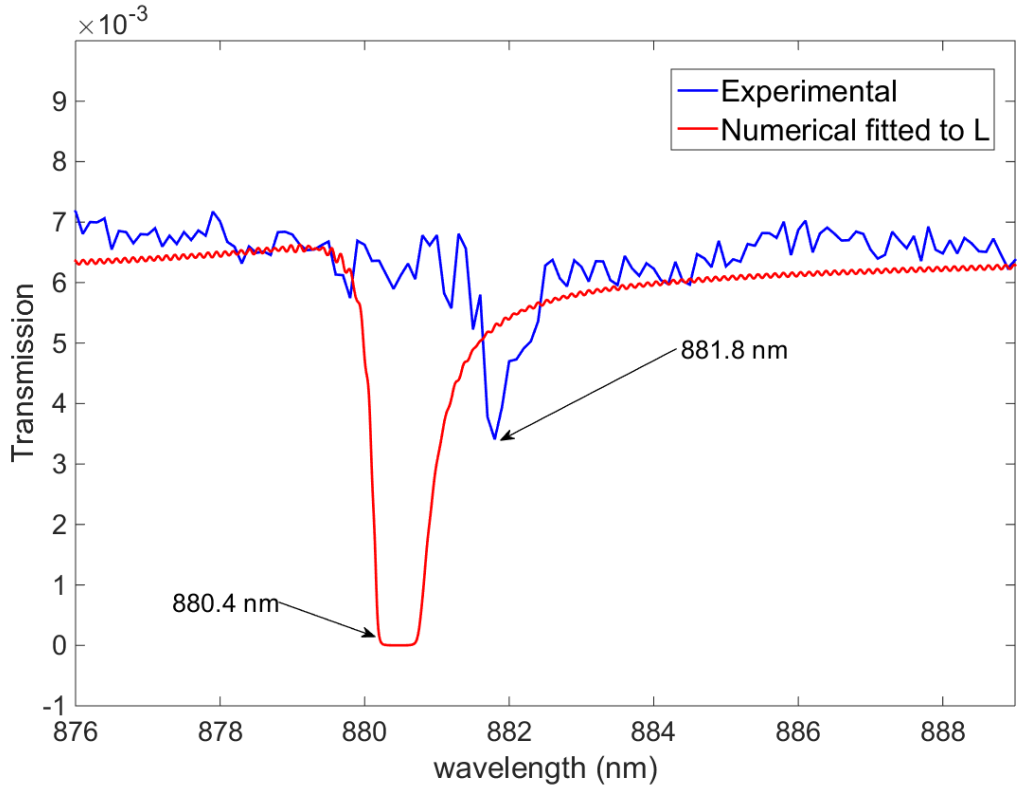

Figure 34 Experimental transmittance compared to the numerical transmittance obtained from TMM and fitted to the estimated L coefficient for a pitch Λ_2= 303 nm, measured to be L=0.08.

As can be seen in Figure 33 and Figure 34, the numerical and experimental Bragg wavelengths don't match perfectly, the experimental presenting a small red shift. Also, the transmitted signal at λ_B calculated theoretically is almost zero, whereas there is only a 50% reduction in the transmitted signal at λ_B compared to the averaged transmission off resonance. Furthermore, the measured transmittance curve, especially for design 1, is far from the smooth appearance given by the numerical results. Some peaks (see Figure 33, λ=854 nm), that cannot be identified as noise due to their repeated presence in every measurement, are clear demonstrations of grating imperfections. Table 2

compares parameters from the numerical and experimental transmission curves. The transmission drop is defined as:

$$Transmission\ drop = \frac{T_{\lambda_B}}{T_{ave}} * 100\% \qquad 46)$$

where T_{ave} is the average transmission of the PPBG off of the Bragg wavelength.

Table 2 Grating characteristics for design 1 and 2, given by numerical and experimental results

Characteristics	Λ_1 numerical	Λ_1 exp	Λ_2 numerical	Λ_2 exp
λ_B [nm]	851.6	854.9	880.4	881.8
Transmission drop [%]	0.01	≈55	0.01	≈53

Looking at these results, one can easily see the discrepancies in performance between the theoretical values and the measured ones. These results are discussed and a tentative explanation for the discrepancies will be provided in what follows.

Bragg gratings are defined by many parameters, each subject to variations due to limitations in fabrication control. The length (d_i) and width (w_i) of each section in the Bragg are limited to the accuracy of the E-Beam system.

A statistical value of the section length d_i and the section width w_i could be obtained from exhaustive AFM analyses to extract the standard deviation in these two parameters. This standard deviation could be included in the numerical study of the

Bragg performance and a more accurate model would be obtained but this would be tedious work.

The section width determines the effective refractive index of the section. A different value than the one used for the theoretical calculations could result in a different effective index, thus affecting the Bragg performance. If the small width section is wider than predicted, its effective index is bigger than expected, the perturbation in effective refractive index will decrease the quality of the Bragg as a reflector.

An E-Beam signal too strong during writing would produce Bragg structures that have a sinusoidal-like profile instead of a perfect step square shape. This sinusoidal profile (caused by over-exposure) greatly decreases the grating performance since it changes entirely the width and the steps in width. On the contrary, a weak E-Beam signal (providing an under-exposed sample) gives deformed triangular shaped sections with a width w_1 smaller than anticipated. This case scenario would also reduce the grating strength (Δn). Figure 35 shows two cases of PPBG malformation due to under (left) or over (right) exposure.

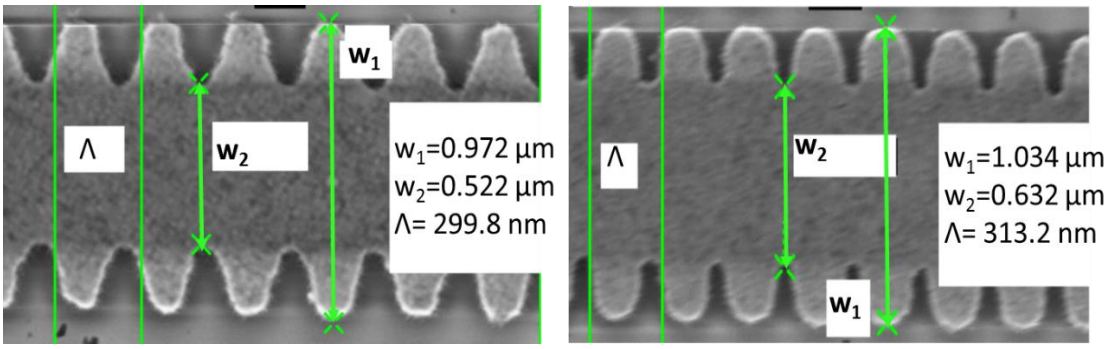

Figure 35 SEM images of PPBGs with low (left) or high (right) exposure to E-Beam. The shapes obtained for the gratings are either triangular (low exposure) or sinusoidal (high exposure) and the PPBG performance is sub-optimal.

As for structures achieving the desired teeth-like shape, there could still be some differences between the expected design and the obtained one, as seen in Figure 36

where the pitch of both designs 1 and 2 are a couple of nanometers longer or shorter and the width w_2 is larger than anticipated.

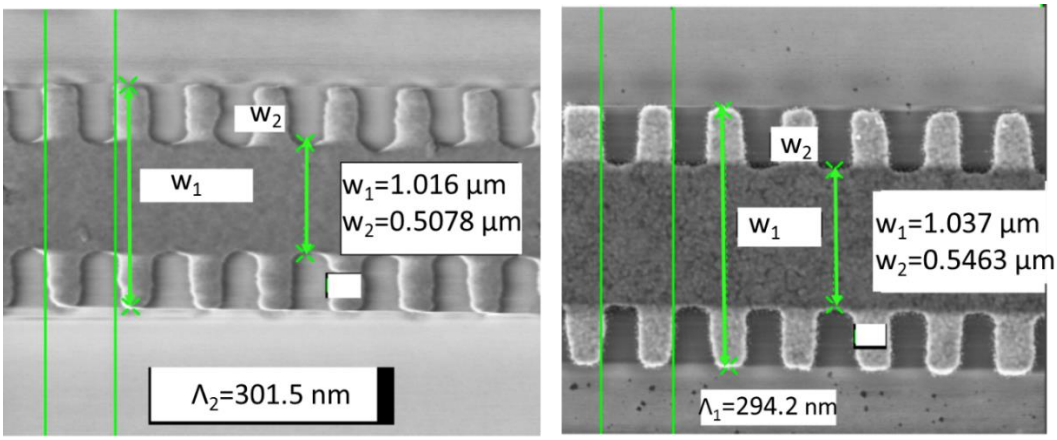

Figure 36 SEM images of sections of gratings 1 and 2

Furthermore, the liftoff of the resist layer to define the gold grating might remove or bend some of the gold, since gold has a weak adhesion to SiO_2. The resulting defects, which can be observed via AFM as shown in Figure 37, is a grating whose teeth have "wings" elevated in comparison with the rest of the grating (therefore appearing approximately 10 nm thicker than the rest of the grating from the AFM topography study). A solution is to deposit a layer of chrome with thickness less than 2 Å between the SiO_2 and gold layers. This technique is known to improve the gold adhesion while increasing the attenuation. Unfortunately, the devices containing chrome that were available for this work showed signs of islandisation and the Bragg gave no promising results due to this defect of fabrication.

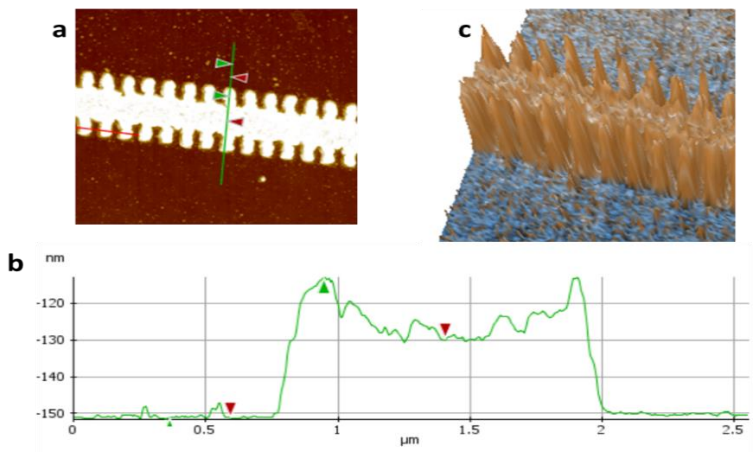

*Figure 37 AFM imaging of a grating with bad adhesion at its teeth. **b** is the thickness profile along the green line of **a**, while **c** is a 3-D image.*

The effective index values of each section $\tilde{n}_{eff1}$ and $\tilde{n}_{eff2}$, used for modelling the Bragg reflection and transmission curves, are calculated numerically (using Comsol) and depend on the refractive index of each layer (SiO_2, gold, PMMA, air). These refractive indices were obtained from sources rather than measured experimentally for each specific material (*e.g.*, using an ellipsometer). To implement this step in the procedure would provide a more accurate value of each material refractive index, thus a more accurate and specific theoretical result of the transmission and reflection curves for the Bragg gratings.

Another possible reason for the weak performance of the Bragg gratings would be the presence of significant background light due to a poor input coupling factor. The low coupling factor might be caused by a mode mismatch between the mode exiting the 100 X objective lens and the LRSPP mode (which is expected to be about 2 µm in diameter). As previously stated, the resolution limit of the available beam profiler (20 µm) prevents its use for direct measurement of the waist diameter. Therefore, the mode field diameter exiting the objective lens and its waist had to be calculated relying on Gaussian beam theory, while the waist position relative to the objective lens was measured using the beam profiler. Assuming that the beam follows Gaussian beam equations, the waist was estimated to be 1.32 µm and be localised at 1.162 mm from

the objective lens with a Rayleigh range of 6 µm (well within the limit of precision for the positioner used for alignment, providing a 0.5 µm fine adjustment). This theoretical value of the waist could be underestimated, resulting in a bigger input mode and a weak coupling to the LRSPP supported mode, creating intense background light that is challenging and tedious to remove from the output signal. This background light would still be present at the Bragg wavelength, thus preventing the experimental transmission from reproducing the theoretical results. This would explain the disparity between the numerical and experimental transmission drops. Measurements using a cleaved fibre were then explored with the objective of improving the mode size matching between the probe signal and the LRSPP mode, since the mode field diameter exiting the polarisation maintaining (PM) fibre is known to be about 6 µm and because of the possibility to add a droplet of index matching fluid between the waveguide and the tip of the fibre, preventing any increase in coupling loss due to facet roughness - this option is not available for the set-up based on an objective lens so the input coupling factor remains high and dependent on the quality of the DUT faces. The updated setup using a cleaved fibre is described in Figure 38.

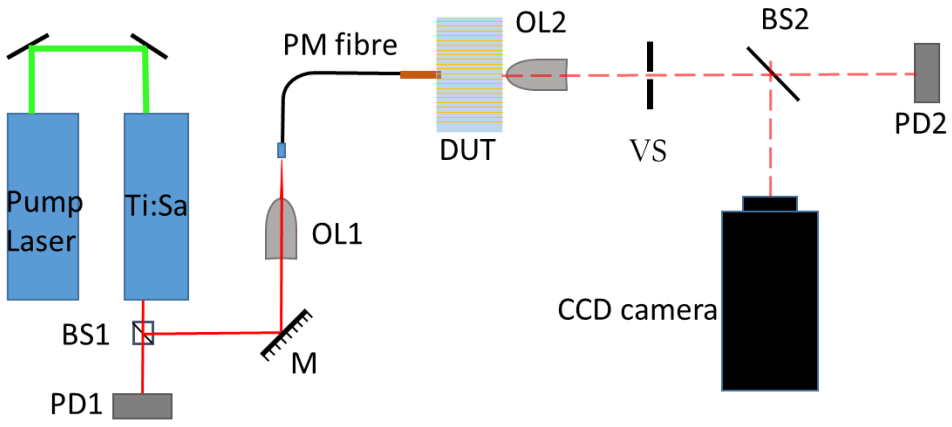

Figure 38 Modified PPBG characterization setup. Solid path: probe beam; broken path: LRSPP mode output. Ti:Sa: Ti:Sapphire laser for probing; BSi: beam splitter; PD: power detector; M: mirror; OL: objective lens; DUT: device under test; VS: variable slit.

The PPBG showing the best performance (with a pitch Λ_2= 303 nm and a transmission drop of 53% at the Bragg wavelength λ_B=881.8 nm) was retested using this new updated setup and the results obtained from this new set of experiments are presented in Figure 39.

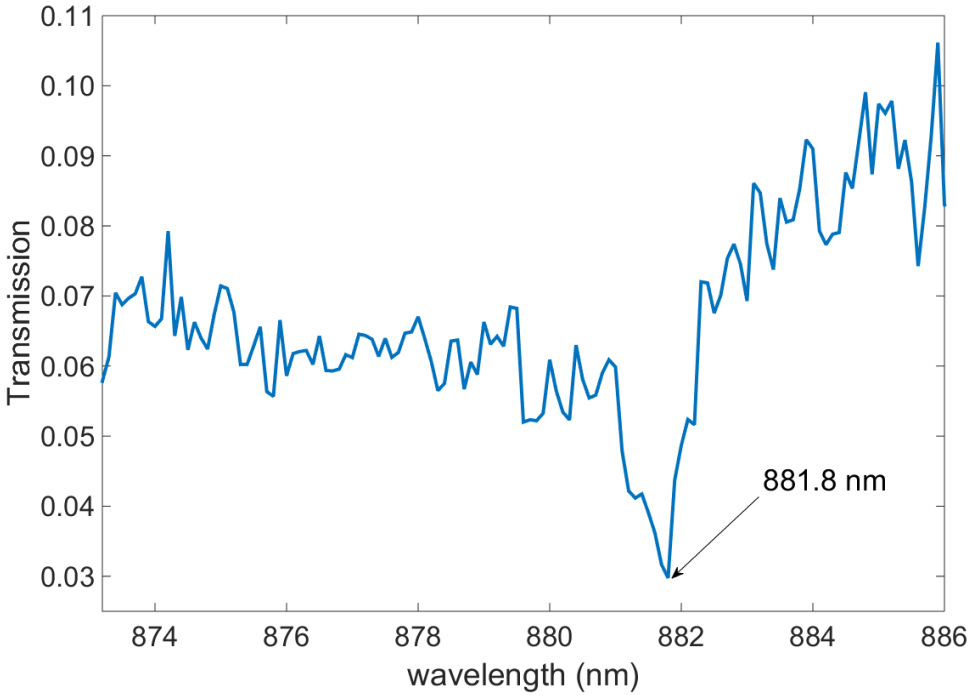

Figure 39 Experimental transmittance for a pitch Λ_2= 303 nm. λ_B=881.8 nm; transmission drop is 45%.

The Bragg wavelength was found to be at λ_B=881.8 nm, invariant from previous measurements, but the Bragg performance was slightly better (with a transmission drop of 45%) than in a free space setup, owing to an improved mode size matching and reduced coupling losses between the probe signal and the LRSPP mode. However, the performance of the PPBG is still weak compared to the expected drop in transmission given by the TMM simulation. The conclusion is that fabrication needs improvement to obtain quality devices.

Some attempts were made to collect the reflected wave signal with a PD3 at the transmission branch of BS2, thus collecting the reflectance curve R as a function of wavelength to verify the theoretical curves calculated via TMM as shown in Figure 25,

Figure 27and Figure 29. No significant peak was observed at λ_B throughout these reflection experiments due to the combined reflection from OL1 and from the PMMA layer of the DUT end facet, hiding the reflected wave from PPBG. More attempts to obtain reflection curves will be made in the near future.

2.5 Conclusion

A new design of PPBG in the near-infrared coated with a solid polymer was successfully tested as possessing a Bragg bandwidth of reflection. Although the grating performance was not as good as the one predicted by theory (calculated via TMM) a dip in transmission at a wavelength close to the Bragg wavelength was observed in two PPBG designs out of three, namely for the pitch of 293 nm (giving a transmission drop of 55% at a Bragg wavelength λ_B=854.9 nm) while the pitch of 303 nm gave a transmission drop of 53% at λ_B=881.8 nm. The setup was changed from a free space to a fibre coupling technique to improve the mode matching. The PPBG with a pitch of 303 nm was tested using this new setup and the transmission drop was found to be improved at the Bragg wavelength of 881.8 nm, transmitting a power of 45% compared to off-resonance transmission. This Bragg performance is still weak in comparison to the expected power drop from TMM calculations. The fabrication of the PPBGs needs some improvements to produce higher quality transmittance and reflectance responses concordant with the modelled curves.

Chapter 3: Gain optimisation and bleaching of IR-140 doped PMMA

3.1 Summary

An in-depth investigation of the gain medium (IR-140 dye doped poly(methyl methacrylate) better known as PMMA) is performed. This gain medium was selected as the gain layer for plasmonic amplifiers and lasers designed by my colleague PhD candidate Elham Karami Keshmarzi. The parameters for maximum gain are determined, a study of the ASE polarisation is performed and bleaching is investigated. This chapter is presented as a manuscript submitted for publication, divided into sections. The first section, *Introduction*, summarises briefly past research on gain obtained from various doped polymer and amplifiers for SPP waves, followed by research conducted by my colleague Elham Karami Keshmarzi on IR-140 properties, prior to my own research. The second section (*Structure and approaches*) briefly describes the structures of interest and the numerical method followed to obtain the confinement factor in the structures of interest. Section 3 (*Fabrication*) enumerates the steps to fabricate the device. Section 4, *Experimental method and results*, is divided into subsections each describing the setup and the method followed, as well as the results obtained and their discussion. These subsections are organised as follows: *Thickness profile*, *Spontaneous emission (SE)*, *Gain measurements*, *Polarisation study of the ASE signal* and *Bleaching test*. The article ends with section 5 (*Conclusion*) that summarizes the results.

3.2 Contributions

The samples tested in this investigation were fabricated by PhD candidate Elham Karami Keshmarzi. I designed and built the experimental setup, I acquired the experimental results and interpreted them. I also computed the confinement factor of the structures and wrote the first draft of the manuscript. Dr. Berini contributed to the

interpretation of the results and revised the manuscript, and Dr. Tait also revised the manuscript.

3.3 Article

The manuscript that follows has been submitted to AIP advances.

Gain optimisation and bleaching of IR-140 doped poly(methyl methacrylate) (PMMA)

Maude Amyot-Bourgeois[1], Elham Karami Keshmarzi[23], Niall Tait[2], and Pierre Berini[134]

[1] *Department of Physics, University of Ottawa, Ottawa, K1N 6N5, Canada*

[2] *Department of Electronics, Carleton University, 1125 Colonel by Dr., Ottawa, K1S 5B6, Canada*

[3] *School of Electrical Engineering and Computer Science, University of Ottawa, 800 King Edward Ave., Ottawa, K1N 6N5, Canada*

[4] *Centre for Research in Photonics at the University of Ottawa, Ottawa, K1N 6N5, Canada*

The optimal IR-140 weight ratio concentration producing maximum gain in amplified spontaneous emission measurements in the near-infrared (~880 nm) is determined. The structures investigated consist of PMMA polymer thin films, doped with IR-140 dye molecules in 4 different concentrations (0.7%, 0.8%, 0.9% and 1.0%), spin-coated on a silica layer grown on silicon wafers. The maximum gain obtained is g = 81 cm^{-1} for the 0.9% weight ratio sample. The polarisation dependence of the gain medium was also investigated and found to be similar in the TE and TM orientations. Bleaching of the gain medium, characterized by a decrease in the available gain, was also explored and found to be rapid for thin films. However, bleaching is reduced as the pump energy density is reduced, creating a trade-off between gain and film longevity. The gain films can be structured via e-beam lithography, are easily integrated with many materials, and should prove useful for demonstrating device ideas and concepts in plasmonics and nano-photonics.

I. INTRODUCTION

Solid state gain media are favourable compared to gain media in solutions, as they do not present any issues brought by flowing liquids such as the need for fluidic channels, irregular flow rate or evaporation. Polymers doped with gain material are interesting because of the ease with which they are integrated with other materials and optical structures as a solid state high gain material pumped optically. Much research has been conducted on amplified spontaneous emission

(ASE) gain from doped polymers in the visible range such as conjugated polymer BuEH-PPV[1] or in the near-infrared (NIR) such as poly(vinyl-pyrrolidone) (PVP) doped with LDS798[2].

A polymer of particularly strong interest is poly(methyl metacrylate) (PMMA) for its low cost and ease of fabrication through well-known spin-coating and curing processes. Furthermore, its chained molecular structure makes PMMA a common choice amongst positive tone resists used for electron-beam lithography in nanofabrication of waveguides, gratings and nanoantennas. Other qualities worth mentioning are its good optical transparency and high thermo-optic coefficient ($dn/dT_{PMMA} = -1.1*10^{-4}$ K^{-1}), making it a good candidate as a solid state polymer integrated with thermally-tunable optical components. Many ASE gain studies in the visible range have been performed on PMMA doped with various dyes such as Disperse Orange 11[3], pyrromethene 567[4] and Rhodamine 6G[5,6] but there remains few studies of the ASE of dye-doped PMMA in the NIR. The organic dye IR-140 is an attractive option as an active dopant in the NIR because its wide emission spectrum peaks around 880 nm. A study previously done[7] integrated IR-140 in a PMMA polymer matrix to study the ASE and measured a gain of 6.6 cm^{-1} at an emission wavelength varying from 920 to 970 nm. Researchers[8] investigated the effects of dye concentration and pump energy density on the gain obtained from IR-140 dye-doped PMMA films used as slab waveguides and found a good molecular weight (m.w.) ratio of 0.8% producing a maximum ASE gain of 68 cm^{-1}.

Long-range surface plasmon polaritons (LRSPPs) are surface waves propagating at the interfaces between a thin metal film and a dielectric. One limitation to the application of LRSPPs is the propagation loss. It has been proposed[9] to obtain loss compensation of SPP modes by using a gain medium as the cladding. Since then, numerous studies[10,11,12,13,14] have been performed on loss compensation, amplification and stimulated emission of SPPs. The SPP propagation losses diminish as the wavelength increases, due to a reduction of the metal absorption. Therefore, the overcompensation of SPP loss (SPP amplification) is easier in the NIR. A study[15] selected IR-140

as the dopant in a solution consisting of a mixture of ethylene glycol and dimethyl sulphoxide used to cover a 1 μm wide gold waveguide, and the structure was pumped optically from the top to produce LRSPP amplification. A subsequent study[16] investigated LRSPP gain on a thin gold film symmetrically bounded by two layers of IR-140 dye-doped PMMA. LRSPPs have a lower attenuation than other SPP waves, and because of this, LRSPPs are good candidates towards the realisation of single-mode plasmonic lasers[17,18].

This paper builds on a previous study[8] investigating the potential and properties of IR-140 dye as an active dopant in PMMA (Poly(methyl methacrylate)) for LRSPP amplifiers and lasers. We investigate the gain performance of thin films (1 μm), close to the thickness of the gain medium required in recently-proposed LRSPP lasers[18], by carrying out amplified spontaneous emission (ASE) measurements. Four concentrations of IR-140 in PMMA were tested and compared for different pump intensities, leading to optimal parameters maximising the material gain available from this system. The polarisation dependence of the gain is also investigated. Furthermore, using a new set-up comprising a spectrograph and a high-speed intensified camera we acquire a sequence of individual single-pulse measurements allowing an accurate assessment of the photo-bleaching of the films.

The paper is organised as follows: We first describe the structure of interest and the approaches, and give a brief overview of the fabrication steps. We then proceed to describe the experimental setup and techniques applied to measure the material gain in each structure, we summarise and discuss the results, and end with concluding remarks.

II. STRUCTURE AND APPROACHES

The structure of interest, sketched in FIG. 1(b), consists of a film of PMMA doped with IR-140, supported by a layer of SiO_2 and covered by air. The film is inserted in a variable slit (VSL) set-up, as sketched in FIG. 1(a), which varies the length of the pumped waveguide while monitoring the output intensity to extract the modal gain via ASE (discussed in detail below). The experiments

were conducted on PMMA films of two different thicknesses: t_{PMMA} =4 and 1 µm, of different IR-140 concentrations (0.7%, 0.8%, 0.9% and 1.0%) and for varying pump intensities. An investigation of the ASE polarisation is carried out, as well as a study of the bleaching for both film thicknesses. FIG. 1(c) shows the output facet of a sample, captured using an IR-camera under pumping, revealing the ASE signal generated in the structure (and showing some directly scattered pump light).

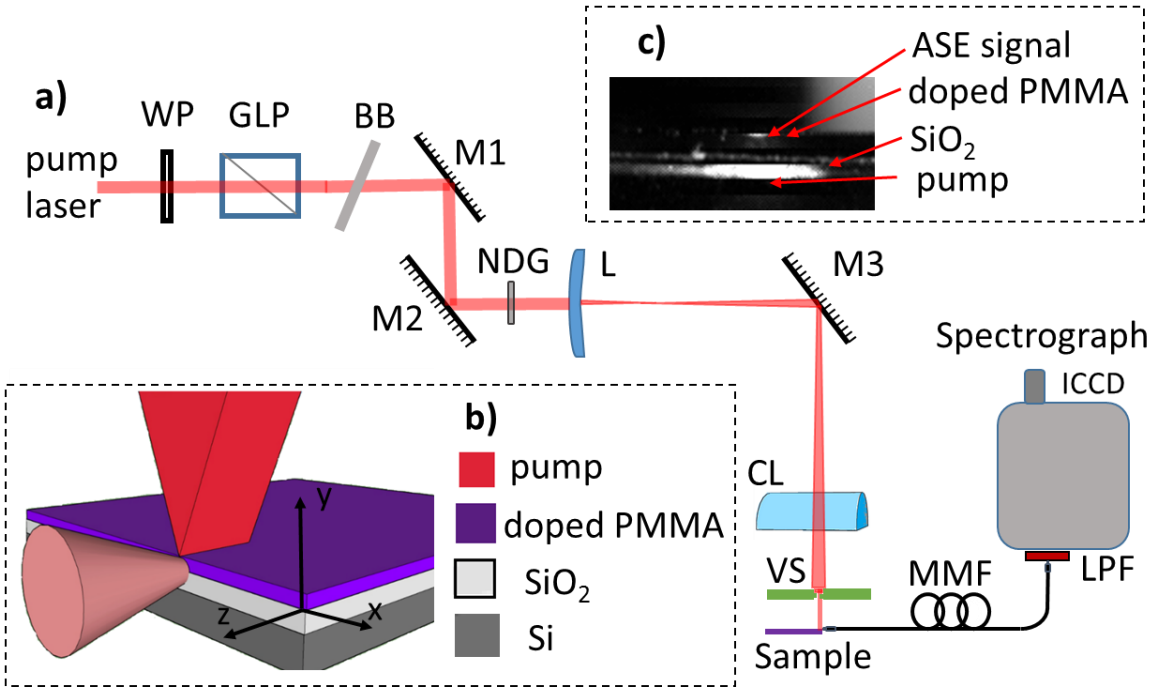

FIG. 1. a) Experimental setup. WP: wave plate; GLP: Glan-Laser Polariser; BB: motorized beam blank; M_i: silver mirrors; NDG: neutral density glass; L: plano-convex lens; CL: cylindrical lens; VS: variable slit; MMF: multimode fibre; LPF: 850 nm long pass filter. b) 3D sketch of a sample structure with pump stripe and ASE signal. A coordinate system was added for clarity. The pump stripe length extends along the z axis. c) Imaging of the ASE signal with a CCD camera.

The variable slit length method used to measure the gain in the doped medium gives the modal gain g_{mod}, from the intensity equation:

$$dI_{ASE}/dz = (CF \times g_{mat} - \alpha)I + J \;\; = \;\; g_{mod}\, I + J \qquad (1)$$

where I_{ASE} is the ASE signal intensity, J is the photon spontaneous emission factor, g_{mat} and g_{mod} are respectively the material and modal gains, and α, the attenuation constant, is neglected due to the low propagation loss encountered over short distances z. g_{mat} can then be extracted from:

$$g_{mat} = g_{mod}/CF \qquad (2)$$

The confinement factor (CF) of this structure is defined as the ratio of the mode power in the doped PMMA layer to the total mode power in the structure (PMMA, air and SiO_2) and can be expressed as:

$$CF = \int_0^{t_{PMMA}} S_{ave} dy \,/\, \int_{-\infty}^{\infty} S_{ave}\, dy \qquad (3)$$

where t_{PMMA} is the doped PMMA layer thickness (along the y axis) and S_{ave} is the power density associated with the TE_0 mode (E_x) or TM_0 mode (E_y), expressed as:

$$S_{ave} = \frac{1}{2} Re\left\{(\vec{\boldsymbol{E}} \times \vec{\boldsymbol{H}}) \cdot \hat{z}\right\} \qquad (4)$$

The CF was calculated numerically from the electric field norm distributed over the device cross-section, obtained from finite-element modelling of the vector wave equations (Comsol), then discretizing the integration domain into finite elements on which the electric field magnitude E_x or E_y were extracted. Equation (3) was then approximated as:

$$CF_{x,y} \approx \sum_j Re\{\left|E_{x,y\ j\ PMMA}\right|^2\} \,/\, \sum_j Re\{\left|E_{x,y\ j\ PMMA+SiO2+air}\right|^2\} \qquad (5)$$

where $E_{x\,j}$ (TE_0 mode) and $E_{y\,j}$ (TM_0 mode) are 1D-matrix elements for which the absolute square is calculated.

FIG. 2 shows the distribution of the $E_{x\,j}$ and $E_{y\,j}$ fields as they vary along the y coordinate for a sample wafer with a PMMA layer thickness of 1 μm. At this thickness the confinement of the

slab modes propagating therein is not very high and a non-negligible portion of the fields propagate in the passive substrate (of lower refractive index than the active film).The calculated CF for this specific structure was CF_{TM0} =0.5092 (which remains constant for a PMMA thickness variation of ±30 nm) and CF_{TE0} =0.6038 (which remains constant for a PMMA thickness variation of ±40 nm). These calculated values of CF are used to calculate g_{mat} from the measured g_{mod} in each structure characterised using equation (2). The CF in the case of the t_{PMMA}=4 µm thick films is very close to 1.

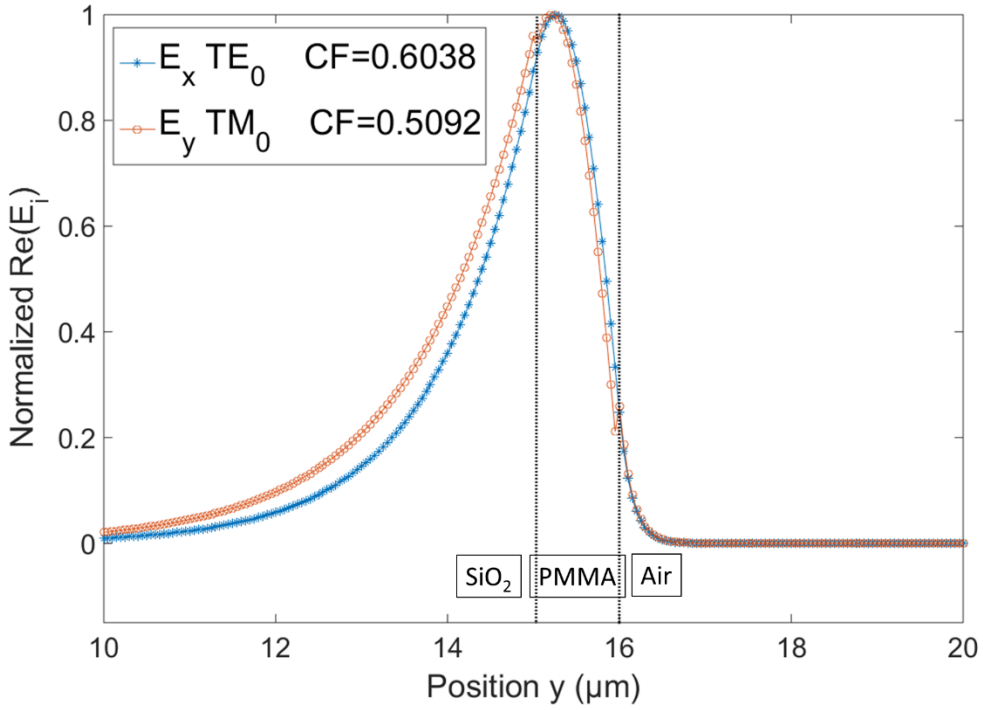

FIG. 2. Simulated distribution of the normalized electric field magnitude along the y axis of the film structure. CF is the confinement factors calculated for TM_0 and TE_0 modes for the case t_{PMMA} = 1 µm.

III. FABRICATION

Previously[8], dye-doped PMMA films with dye molecular weight (m.w.) ratios of 0.4%, 0.8%, 1.2% and 1.6% were fabricated and tested, and it was found that the 0.8% concentration film produced the highest material gain among this set[8]. Therefore, here we limit our concentrations to near 0.8% in order to determine an optimum. The four weight ratios of IR-140 to PMMA solids were selected as 0.7% (4.6×10^{18} cm^{-3} molecular concentration), 0.8% (5.2×10^{18} cm^{-3}), 0.9%

(5.9×10^{18} cm^{-3}) and 1% (6.5×10^{18} cm^{-3}). The IR-140 dye has a broad absorption peak around 819 nm and a narrower fluorescence emission peak around 880 nm. The IR-140 dye was diluted in PMMA dissolved in dichloroethane. The four different dye-doped PMMA solutions were then spin-coated on a 15 µm thick SiO_2 layer on 500 µm thick Si substrates. The spinning speed (RPM) determines the final thickness of the doped PMMA layer on the wafers. To avoid the effects resulting from the edge bead created during the spinning process, the wafers were carefully cleaved and then cleaned with isopropyl alcohol. The ASE emission was collected from the clean cleaved edges near the centre of the wafers.

The thickness of each film was then measured using a Dektak profilometer. The sample under test was first carefully scratched along two edges to remove the PMMA layer and create a reference level along the top surface of the SiO_2 layer. Then, a scan was performed monitoring the PMMA thickness from one scratch to the other. The Dektak software allows some post-processing to level the resulting profile (assuming the SiO_2 height is uniform). FIG. 3 shows thickness scans for each sample tested and Table I summarises the average PMMA thickness and the standard deviation, both taken over each scan, for four scans performed on each sample.

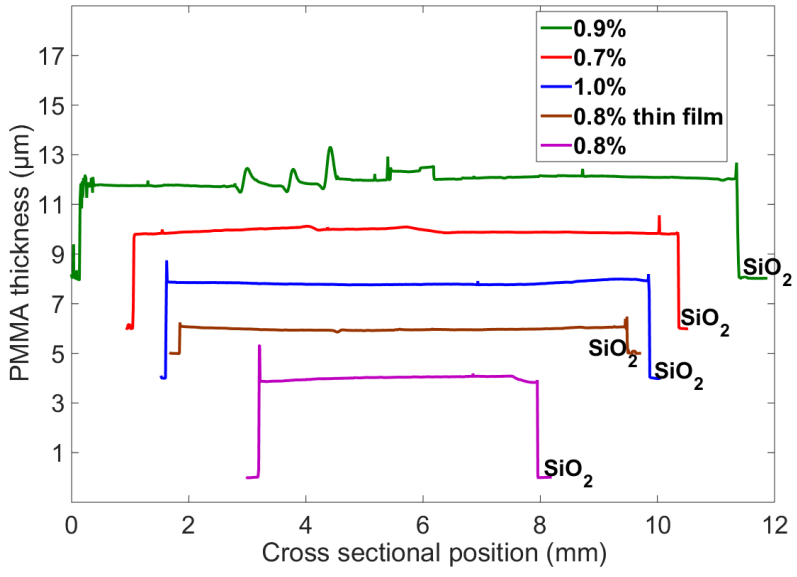

FIG. 3. Thickness of PMMA films doped with different IR-140 weight ratios. The profiles are shifted vertically for clarity. The steps correspond to the height of the PMMA layers relative to the SiO_2 surface.

TABLE I. Average of the thickness profiles (t_{PMMA}) and standard deviation (σ) for each sample concentration.

m.w.	t_{PMMA}	σ	t_{PMMA}	σ	t_{PMMA}	σ	t_{PMMA}	σ
%	μm	μm	μm	μm	μm	μm	μm	μm
0.7	3.95	0.08	3.9	0.2	3.95	0.09	4.05	0.05
0.8	3.78	0.05	3.97	0.09	4.01	0.06	3.83	0.05
0.9	3.9	0.4	4.6	0.5	3.6	0.4	4.0	0.2
1.0	3.80	0.06	3.71	0.08	3.7	0.1	3.67	0.09
0.8 thin	0.90	0.04	0.93	0.05	1.02	0.05	0.97	0.04

IV. EXPERIMENTAL METHODS AND RESULTS

A. Spontaneous emission (SE)

The four samples of different IR-140 concentration were illuminated using a Centennia CW laser system emitting at 532 nm. A small fraction of the beam power was coupled into a multimode fibre and redirected to a 10× objective lens to focus the beam onto the top surface of a sample. The spontaneous emission was collected from a cleaved edge using a multimode fibre and sent to an optical spectrum analyzer, (Newport, model OSM2-400VIS/NIR). A sample SE spectrum is shown in the inset of FIG. 4, revealing peak emission near 880 nm.

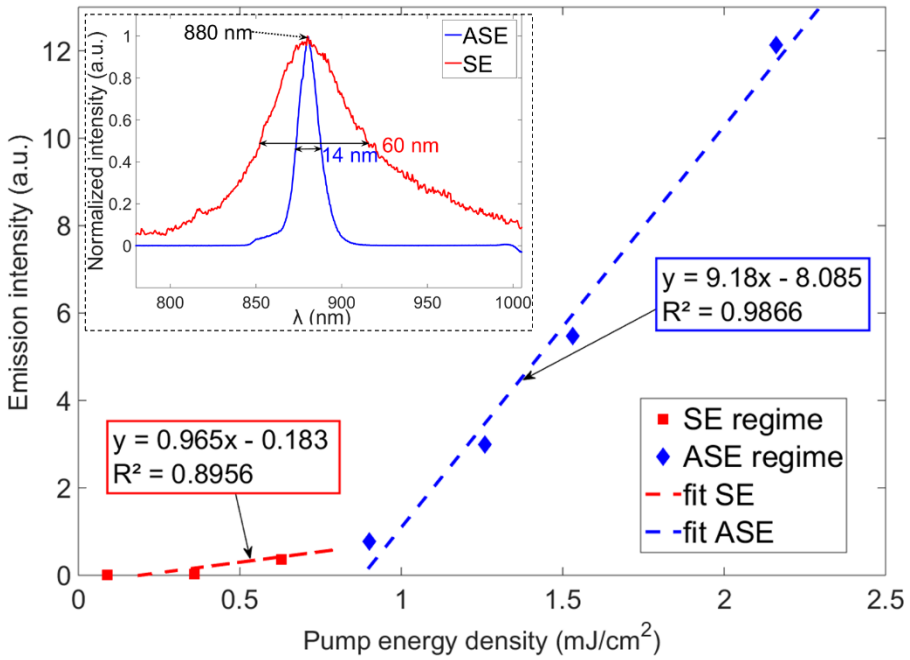

FIG. 4. Emission intensity as a function of pump energy density, showing energy threshold for ASE. Inset: comparison between fluorescence (SE, low pump energy density) and ASE (pump energy density E_p=3.6 mJ*cm^{-2}) spectra. Sample: 0.9% IR-140 and t_{PMMA} = 4 µm.

B. Gain measurements

The pump signal for the gain measurements was generated via a Cobra Stretch Sirah pulsed dye laser system using a solution of styryl dye emitting at 810 nm. The dye laser was pumped using a Quanta-Ray PRO-Series pulsed Nd:YAG laser from Spectra-Physics, with a repetition rate of 10 Hz. A detailed schematic of the experimental setup is shown in FIG. 1 (a). Using a wave plate (WP) and a Glan Laser polariser (GLP), the laser average power could be varied. Neutral density glass (NDG) was added to the system for further attenuation of the pump signal, to prevent saturation in the ASE signal and burning.

Prior to installing the lenses and the variable slit (VS) in the setup, it was important to ensure that the pump beam was perpendicularly incident on the sample surface. This was performed by placing a gold plated mirror at the sample location, then adjusting the orientation of mirror (M3) until the reflection from the gold mirror was collinear with the pump beam along the beam path. Once this was accomplished, the lenses (L and CL) and the VS were added to the system.

The pump beam after the attenuation section (NDG) was expanded with a lens (L) then a mirror (M3) directed the beam down toward the sample through a cylindrical lens (CL) to transform the pump circular beam into a narrow width stripe along the z orientation of the sample, as sketched in FIG. 1 (b).

The sample distance from the cylindrical lens was chosen such that the pump stripe width measures 100 to 150 μm. The pump polarisation was aligned parallel to the length of the pump stripe (z axis) throughout the experiments because it is in this orientation that the TM mode has the strongest gain coefficient and emission intensity (SPP waves are TM in nature), whereas the ASE emission is strongly TE polarised if the pump polarisation is perpendicular to the length of the pump stripe[8].

The variable slit (VS) was placed near the sample to reduce diffraction effects on the pump beam[19]. However, due to physical limitations in the setup, the slit had to be at a certain distance from the sample (although the distance was minimized). The VS was constructed from a micrometer-controlled movable blade and a fixed blade. The slit width can be varied from 0 to 3 mm.

The relation between the VS width and the actual stripe length was determined using photosensitive photographic paper by measuring the stripe length from the burn edges on the paper for various slit widths. A linear equation relating the stripe length to the slit width was estimated and used for the gain measurement experiments. This calibration step had to be performed after each setup modification, because a change in a component position or orientation (for example, moving vertically the CL or the VS) changes the linear relation between the slit width and the stripe length.

Homogeneity of the pump stripe is a key factor for good gain measurements[19]. The homogeneity of the pump stripe intensity over its length was tested by measuring the pump stripe

power incident on the sample position using a power meter for various openings of the slit, varying the stripe length[20]. A homogeneous stripe has a constant ratio of power over stripe length (all other variables being constant). It was found that the power would vary by a factor of 3% on average, showing a homogeneous pump source.

The sample was placed such that the cleaved edge was at the end of the pump stripe and the two overlapped. A pump stripe that ends before the edge of the sample would reduce ASE signal collection considerably due to absorption in the unpumped gain region.

The signal emitted from the sample was collected using a multimode fibre (MMF) aligned to maximize the emission intensity. The signal was then sent to the spectrograph (Princeton Instruments IsoPlane SCT320 and PI-MAX 4 ICCD camera). An 850 nm long-pass filter was placed before the spectrograph's entrance slit to cut the strong 810 nm pump beam and avoid damage to the ICCD sensor. The ICCD camera was linked to the YAG laser trigger to synchronize the opening and closing of the camera shutter with the occurrence of the pump laser pulses (the YAG laser pulse width varies between 6 and 11 ns). This reduces noise and allows for pulse-to-pulse analysis.

ASE signals can be distinguished from SE signals by their spectra, as shown by the narrowing of the spectrum from 60 nm in the SE regime to 14 nm in the ASE regime, in the inset of FIG. 4. Another sign of evolution from SE to ASE is the rapid increase in signal emission intensity above a certain threshold pump energy density (stripe length remaining fixed), as shown in FIG. 4, revealing that the slope of I_{ASE} as a function of E_p is significantly larger (~10×) in the ASE regime compared to the SE regime.

The experimental method used to determine the material gain for our four concentrations of IR-140 to PMMA is the VSL method. Integrating equation (1) over z from 0 to l and assuming $I_{ASE}(z=0) = 0$ gives:

$$I_{ASE} = J/g_{mod}(e^{g_{mod}l} - 1) \quad (6)$$

Several sets of measurements of I_{ASE} as a function of pump stripe length l were fitted to equation (6) for various E_p on each sample. The modal gain was extracted from these fitted equations. The results of these experiments along with the fitted curves are plotted in FIG. 5(a) and (c), for samples having 0.9% IR-140 and a thickness of t_{PMMA} = 4 µm, and 0.8% IR-140 and a thickness of t_{PMMA} = 1 µm, respectively. Each data point on the plots corresponds to the maximum intensity of an emission spectrum averaged over 40 acquisition pulses for a specific stripe length.

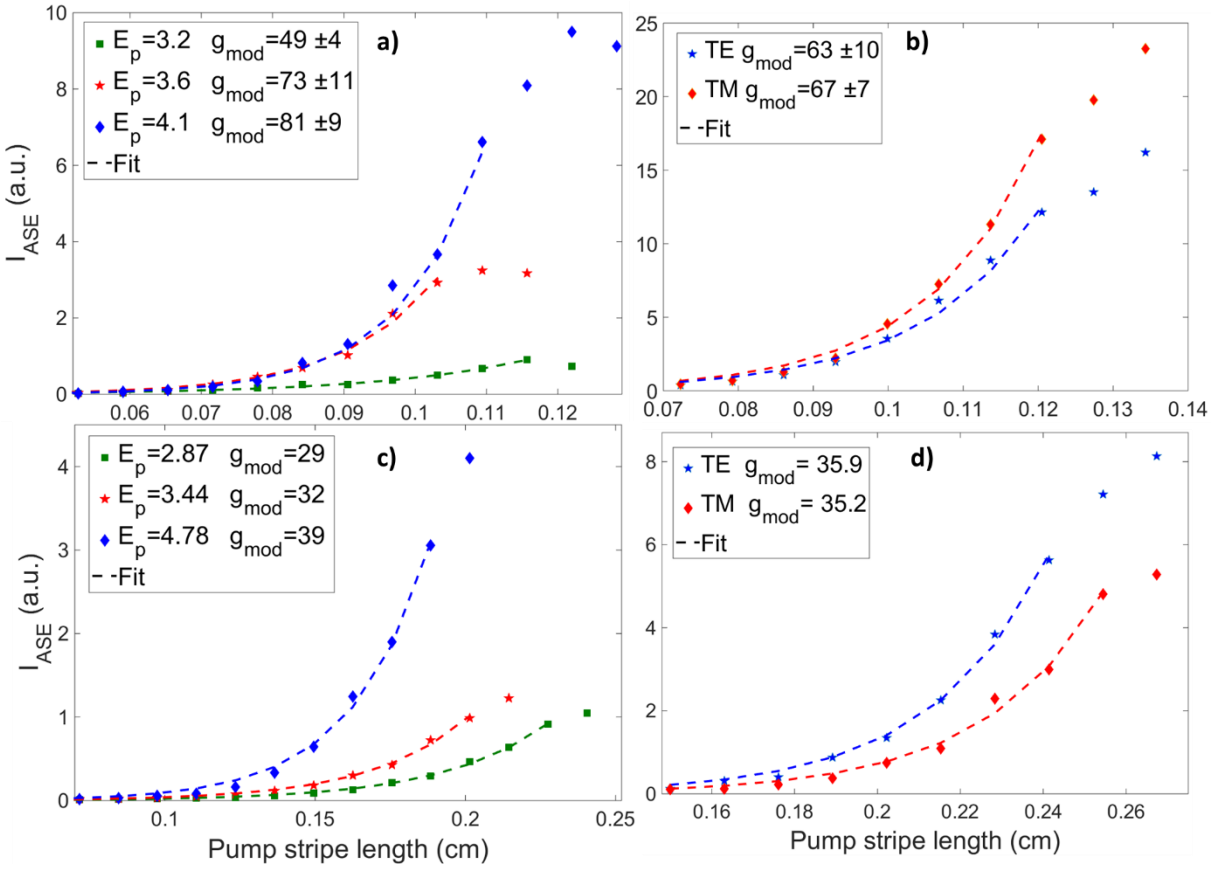

FIG. 5. **a** and **c**: Emission intensities as a function of the stripe length for the sample with 0.9% IR-140 and a thickness of t_{PMMA} = 4 µm (**a**), and 0.8% IR-140 and a thickness of t_{PMMA} = 1 µm (**c**). **b** and **d**: Emission

intensities in the TM and TE orientations as a function of the stripe length for the sample with 0.9% IR-140 and a thickness of t_{PMMA} = 4 µm (**b**), and 0.8% IR-140 and a thickness of t_{PMMA} = 1 µm (**d**). The modal gain g_{mod} (in cm^{-1}) is obtained by fitting Eq. (6) to the measurements. Pump intensities E_p are in mJ/cm^2.

Table II gives the maximum modal gain obtained for each dye concentration at pump intensities below gain saturation. The optimal material gain was produced by the 0.9% m.w. IR-140 concentration at E_p = 4.1 mJ/cm^2, giving a material gain of g_{mat} = 81 cm^{-1}. This is a significant improvement over our previous maximum gain measured for a concentration of 0.8% (g_{mat} = 68 cm^{-1})[8], and confirmed here in Table II for the same concentration (g_{mat} = 70 cm^{-1} for the 4 µm thick film and g_{mat} = 65 cm^{-1} for the 1 µm thick film). The CFs shown in Table II were calculated using the method previously described for TM and TE modes and averaged.

TABLE II. Summary of measured modal and material gains for each sample at its optimal pump energy density; each sample is 4 µm thick except the last one which is 1 µm thick.

Conc., m.w.	E_p	g_{mod}	CF	g_{mat}
[%]	[$mJ*cm^{-2}$]	[cm^{-1}]		[cm^{-1}]
0.7	4.1	72	1	72
0.8	4.5	70	1	70
0.9	4.1	81	1	81
1	4.1	62	1	62
0.8 t=1 µm	4.78	36.2	0.557	65

C. Polarisation study of ASE signal

SPP waves being TM polarised, it is important to determine the material gain that is available in the TM orientation. A polarisation study was conducted to measure g_{mat} in the TM and TE polarisations. The pump polarisation was kept parallel to the pump stripe since it is in this orientation that it was previously demonstrated to possess the strongest TM gain[8]. An analyzer was inserted before the MMF and oriented vertical (TM) or horizontal (TE) for the VSL experiments, measurements for each stripe length being obtained in the two orientations subsequently. The fitted curves for these investigations are shown in FIG. 5(b) and (d) for samples having 0.9% IR-140 and a thickness of t_{PMMA} = 4 µm, and 0.8% IR-140 and a thickness of t_{PMMA} = 1 µm, respectively. Table

III gives the modal and material gains measured in the TE and TM orientations, along with CF calculated using the method previously described. For thick PMMA films the signal is contained within the PMMA layer while for thinner films the confinement is reduced. The TE and TM material gains are observed to be similar.

TABLE III. Summary of measured polarisation-resolved modal and material gains for each sample at their optimal pump energy density; 0.9% sample is 4 µm thick while 0.8% sample is 1 µm thick.

Conc., m.w.	E_p	g_{mod}	CF	g_{mat}
	[mJ*cm^{-2}]	[cm^{-1}]		[cm^{-1}]
0.9% t=4 µm TE	4.1	63	≈1	63
0.9% t=4 µm TM	4.1	67	≈1	67
0.8% t=1 µm TE	4.9	35.9	0.604	59.5
0.8% t=1 µm TM	4.9	35.2	0.509	69.1

The discrepancy between the g_{mat} results given in Tables II and III for similar measurement conditions could be explained by the setup modifications to perform the polarisation study (given in Table III). Indeed, an analyzer and an objective lens were added before the MMF and this addition could induce loss. Furthermore, the polarisation study was performed a few weeks after the gain optimisation study - the samples may have deteriorated slightly over time.

D. Bleaching Tests

Dye molecules are known to degrade when exposed to intense light. While this property is of little consequence in liquid dye solutions with constant flow, it has major effects on a solid layer of PMMA doped with dye, reducing the gain obtained from the material after long exposure to the pump. Since applications depend on the life expectancy of dye molecules in the doped PMMA layer, the bleaching effect was investigated. The pump source used to perform the bleaching test was the same as for the gain measurements. Samples were exposed to different pump intensities below gain saturation, with a pump stripe length below signal saturation. The exposure time varied between 400 and 500 seconds, and the ASE signal was captured by averaging over 50 spectra to

produce one data point (5 seconds at a pump laser repetition rate of 10 Hz). An analyser was added to the emission collection setup to get a better understanding of bleaching for TE and TM orientations in thin PMMA films. The curves for peak emission intensity as a function of the exposure time were extracted, and fitted to exponential curves:

$$I_{ASE}(t) = I_{ASE0} \times e^{-\tau t} \quad (7)$$

The exposure times necessary for a 1/e reduction in signal intensity ($t_{1/e}$) were determined from these exponential curves. From the results shown in FIG. 6, it is seen that for a sample with a thick 4 µm layer of doped PMMA, bleaching is weak, with a $t_{1/e}$ of over 12 minutes. Samples with a thin 1 µm PMMA layer have a shorter life expectancy. The TM_0 mode has a 1/e lifetime of $t_{1/e,TM}(E_p=5.8\ mJ/cm^2)$ = 65 s only, but $t_{1/e}$ is tripled for lower pump intensities [$t_{1/e,TM}(E_p=4.5\ mJ/cm^2)$ = 180 s], implying a trade-off between material gain and lifetime.

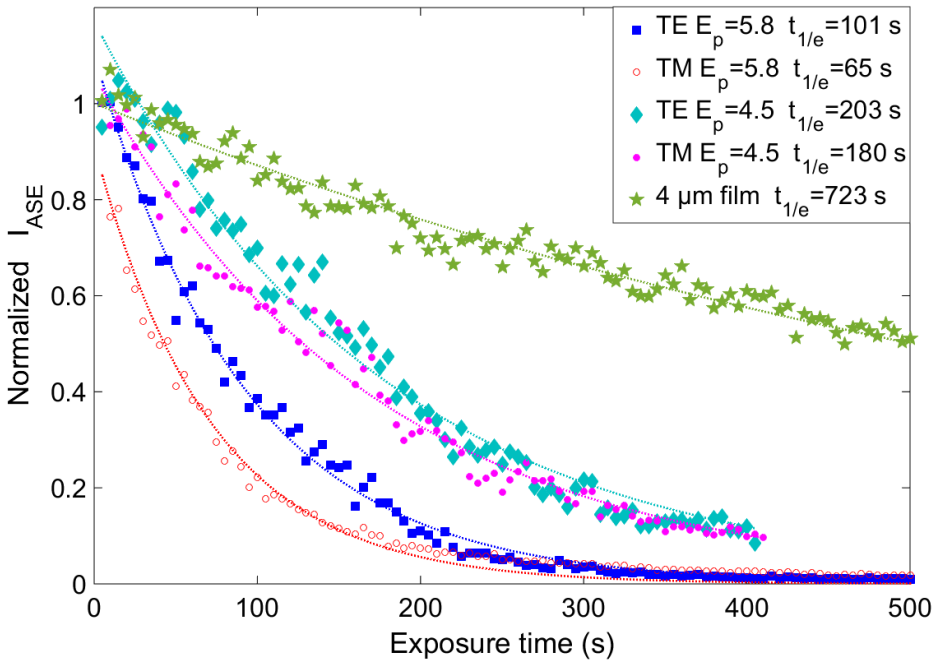

FIG. 6. Bleaching curves of TM and TE modal gains for different pump intensities on the sample with a PMMA thickness of 1 µm, and one bleaching curve for a sample with a PMMA thickness of 4 µm. the $t_{1/e}$ lifetimes of emission given in the figure legend were calculated based on a fitted exponential decay.

V. CONCLUSION

The gain available in PMMA dielectric films doped with IR-140 dye molecules was investigated and a maximum material gain of g = 81 cm^{-1} was measured for an optimal dye molecular weight concentration of 0.9%. The polarisation of the ASE was studied and it was found that the ASE emission is unpolarised, so that the gain available in the TM orientation is sufficient for potential use in single-mode LRSPP lasers. The gain medium life expectancy was measured through a photo-bleaching study to evaluate the practicality of future plasmonic devices incorporating this IR-140 dye doped dielectric cladding.

REFERENCES

[1]McGehee, M. D., Gupta, R., Veenstra, S., Miller, E. K., Diaz-Garcia, M. A., & Heeger, A. J., *Physical Review B* **58**, 7035 (1998).

[2]Yamashita, K., Kuro, T., Oe, K., & Yanagi, H. , *Applied Physics Letters* **88**, 241110 (2006).

[3]Howell, B. F., & Kuzyk, M. G. , *Journal of the Optical Society of America B* **19**, 1790 (2002).

[4]Costela, A., Garcia, O., Cerdan, L., Garcia-Moreno, I., & Sastre, R., *Optics Express* **16**, 7023 (2008).

[5]Somasundaram, G., & Ramalingam, A., *Journal of Photochemistry and Photobiology A: Chemistry* **125**, 93 (1999).

[6]Tou, T. Y., Yap, S. S., Chin, O. H., & Ng, S. W., *Optical Materials* **29**, 963 (2007).

[7]Thompson, J., Anni, M., Lattante, S., Pisignano, D., Blyth, R. I., Gigli, G., & Cingolani, R., *Synthetic Metals* **143**, 305 (2004).

[8]Karami Keshmarzi, E., Tait, R. N., & Berini, P., *Optics express* **22**, 12452 (2014).

[9]Sudarkin, A. N., & Demkovich, P. A., *Soviet physics: Technical physics* **34**, 764 (1988).

[10]Seidel, J., Grafstrom, S., & Eng, L., *Physical Review Letters* **94**, 177401 (2005).

[11]Noginov, M. A., *Journal of Nanophotonics* **2**, 021855 (2008).

[12]Noginov, M. A., Zhu, G., Mayy, M., Ritzo, B. A., Noginova, N., & Podolskiy, V. A., *Physical Review Letters* **101**, 226806 (2008).

[13]Bolger, P. M., Dickson, W., Krasavin, A., Liebscher, L., Hickey, S. G., Skryabin, D. V., & Zayats, V. A., *Optics Letters* **35**, 1197 (2010).

[14]Gather, M. C., Meerholz, K., Danz, N., & Leosson, K., *Nature Photonics* **4**, 457 (2010).

[15]De Leon, I., & Berini, P., *Nature Photonics* **4**, 382 (2010).

[16]Hahn, C., Song, S. H., Oh, C. H., & Berini, P., *Applied Physics Letters* **107**, 121107 (2015).

[17]Jetté-Charbonneau, S., & Berini, P., *Applied Physics Letters* **91**, 181114 (2007).

[18]Karami Keshmarzi, E., Tait, R. N., & Berini, P., *Journal of Applied Physics* **112**, 063115 (2012).

[19]Dal Negro, L., Bettotti, P., Cazzanelli, M., Pacifici, D., & Pavesi, L., *Optics Communications* **229**, 337 (2004).

[20]De Leon, I., & Berini, P., *Review of Scientific Instruments* **82**, 033107 (2011).

Chapter 4: Conclusion

4.1 Thesis conclusions and contributions

In this thesis, two steps toward LRSPP lasers based on PPBGs were accomplished. We investigated the performance in the near-infrared of new passive PPBG designs both numerically and experimentally. The numerical method adopted was the TMM, a common simulation technique applied to compute the response of a dielectric stack model. The experimental setup and procedures were implemented and results were obtained for two PPBG designs. The quality of the Bragg reflectors limited their performance compared to the theoretical results. It was found that two PPBGs out of the three tested possessed a measurable bandgap, which are the PPBG with Λ=293 nm and the PPBG with Λ=303 nm. No bandgap was observed in the PPBG with Λ=313 nm. The reflected wave could not be detected due to high noise background, but the transmitted mode could be monitored, and a transmittance gap (detected as a dip) was detected at λ_B=854.9 nm (close to the numerical λ_B=851.6 nm) for Λ=293 nm and λ_B=881.8 nm (close to the numerical λ_B=880.4 nm) for Λ=303 nm, each transmitting half (≈50%) of the signal off-resonance. The grating with a pitch Λ=303 nm was tested on an improved characterization setup and the PPBG performance was better, showing a transmission drop of about 45%, but the experimental performance is much weaker than the one expected from the TMM simulations. The fabrication techniques, such as the liftoff of the resist, should be optimized to improve the quality of the obtained devices.

The second part of this thesis work consisted of the complete investigation of the performance of IR-140 doped polymer (PMMA), as a novel amplifying medium for future plasmonic devices. The molar concentration and pump intensity giving maximum

material gain were identified experimentally as 0.9% m.w. and I_p=4.1 mJ/cm^2 to obtain a modal gain of g_{mod}=81 cm^{-1}. A polarisation study was conducted showing that the ASE signal was unpolarised, therefore enough gain is available in the TM orientation for stimulated emission and amplification of LRSPP waves, both in thick (t_{PMMA}=4 µm) and thin (t_{PMMA}=1 µm) doped dielectric films. Finally, the life expectancy of the gain medium was studied carefully in bleaching tests, showing that for higher pump intensity, the lifetime $t_{1/e}$ for the TM mode is about 45 seconds, while its longevity can be greatly increased ($t_{1/e}$=200 seconds) for a slightly lower pump intensity, creating a trade-off between gain and longevity.

4.2 Future work

The PPBG transmission curves show promising results, but they are noisy and not as good as expected. Also no reflection curve could be collected due to the heavy presence of background light due to reflections in the set-up and from the DUT. Similar experiments as what was conducted and presented in this thesis should be performed, but replacing the objective lens coupling system with a PM fibre and index matching fluid, also operating in the principles of end-fire coupling. We are hoping to get better transmission results and to see a peak reflection at Bragg wavelengths in this new configuration.

The planned LRSPP lasers based on a DFB given by a uniform periodic first order PPBG are currently being tested by my colleague, PhD candidate Elham Karami Keshmarzi.

References

1. Kittel, C. (1986). *Introduction to Solid State Physics sixth Edition.* Toronto: John Wiley and Sons.

2. Berini, P. (1999). Plasmon-polariton modes guided by a metal film of finite width. *Optics Letters* ***24***, 1011.

3. Berini, P. (2000). Plasmon-polariton waves guided by thin lossy metal films of finite width: Bound modes of symmetric structures. *Physical Review B* ***61***, 10484.

4. Berini, P. (2001). Plasmon-polariton waves guided by thin lossy metal films of finite width: Bound modes of asymmetric structures. *Physical Review B* ***63***, 125417.

5. Maier, S. A. (2007). *Plasmonics: Fundamentals and Applications.* New York: Springer.

6. Ghamsari, B. G., Olivieri, A., Variola, F., & Berini, P. (2014). Enhanced Raman scattering in graphene by plasmonic resonant Stokes emission. *Nanophotonics* ***3***, 363.

7. Krupin, O., Asiri, H., Wang, C., Niall Tait, R., & Berini, P. (2013). Biosensing using straight long-range surface plasmon waveguides. *Optics Express* ***21***, 698.

8. Krupin, O., Wang, C., & Berini, P. (2014). Selective capture of human red blood cells based on blood group using long-range surface plasmon waveguides. *Biosensors and Bioelectronics* ***53***, 117.

9. Wong, W. R., Krupin, O., Sekaran, S. D., Adikan, F. R., & Berini, P. (2014). Serological diagnosis of dengue infection in blood plasma using long-range surface plasmon waveguides. *Analytical chemistry* ***86***, 1735.

10. Krupin, O., Wang, C., & Berini, P. (2015). Detection of leukemia markers using long-range surface plasmon waveguides functionalized with Protein G. *Lab on a Chip* ***21***, 4156.

11. Béland, P., Kruping, O., & Berini, P. (2015). Selective detection of bacteria in urine with a long-range surface plasmon waveguide biosensor. *Biomedical Optics Express* ***6***, 2908.

12. Hecht, E. (2005). *Optique.* Paris: Pearson Education.

13. Saleh, B. E., & Teich, M. C. (2007). *Fundamentals of Photonics.* New Jersey: Wiley.

14. Yeh, P. (1988). *Optical Waves in Layered Media.* New York: Wiley .

15. Jetté-Charbonneau, S., Charbonneau, R., Lahoud, N., Mattiussi, G. A., & Berini, P. (2005 a). Bragg Gratings Based on Long-Range Surface Plasmon-Polariton Waveguides: Comparison of Theory and Experiment. *Journal of Quantum Electronics* ***41,*** 1480.

16. Bozhevolnyi, S. I., Boltasseva, A., Sondergaard, T., Nikolajsen, T., & Leosson, K. (2005). Photonic bandgap structures for long-range surface pasmon polaritons. *Optrics Communications* ***250***, 328.

17. Jetté-Charbonneau, S., & Berini, P. (2006). Theoretical performance of Bragg gratings based on long-range surface plasmon-polariton waveguides. *Journal of Optical Society of America **23***, 1757.

18. Jetté-Charbonneau, S., Charbonneau, R., Lahoud, N., Mattiussi, G., & Berini, P. (2005 b). Demonstration of Bragg gratings based on long-ranging surface plasmon polariton waveguides. *Optics Express **13***, 4674.

19. De Leon, Israel, & Berini, Pierre (2008). Theory of surface plasmon-polariton amplification in planar structures incorporating dipolar gain media. *Physical Review B **78***, 161401.

20. Berini, P., Charbonneau, R., Lahoud, N., & Mattiussi, G. (2005). Characterization of long-range surface-plasmon-polariton waveguides. *Journal of Applied Physics 98*, 43109-1-43109-12.Sudarkin, A. N., & Demkovich, P. A. (1988). Excitation of surface electromagnetic waves on the boundary of a metal with an amplifying medium. *Soviet physics: Technical physics **34***, 764.

21. Sudarkin, A. N., & Demkovich, P. A. (1988). Excitation of surface electromagnetic waves on the boundary of a metal with an amplifying medium. *Soviet physics: Technical physics **34***, 764.

22. Milonni, P. W., & Eberly, J. H. (1988). *Lasers.* New York: Wiley.

23. De Leon, Israel, & Berini, Pierre (2010). Amplification of long-range surface plasmons by a dipolar gain medium. *nature photonics **37***, 382.

24. Seidel, J., Grafstrom, S., & Eng, L. (2005). Stimulated Emission of Surface Plasmons at the Interface between a Silver Film and an Optically Pumped Dye Solution. *Physical Review Letters **94***, 177401.

25. Grandidier, J., Colas des Francs, G., Massenot, S., Bouhelier, A., Markey, L., Weeber, J.-C., . . . Dereux, A. (2009). Gain-Assisted Propagation in a Plasmonic Waveguide at Telecom Wavelength. *Nano Letters **9***, 2935.

26. Bolger, P. M., Dickson, W., Krasavin, A., Liebscher, L., Hickey, S. G., Skryabin, D. V., & Zayats, V. A. (2010). Amplified spontaneous emission of surface plasmon polaritons and limitations on the increase of their propagation length. *Optics Letters **35***, 1197.

27. Noginov, M. A., Zhu, G., Mayy, M., Ritzo, B. A., Noginova, N., & Podolskiy, V. A. (2008). Stimulated Emission of Surface Plasmon Polaritons. *Physical Review Letters **101***, 226806.

28. Noginov, M. A. (2008). Compensation of surface plasmon loss by gain in dielectric medium. *Journal of Nanophotonics **2***, 021855.

29. De Leon, I., & Berini, P. (2009). Modeling surface plasmon-polariton gain in planar metallic structures. *Optics Express **17***, 20191.

30. Gather, M. C., Meerholz, K., Danz, N., & Leosson, K. (2010). Net optical gain in a plasmonic waveguide embedded in a fluorescent polymer. *nature photonics Letters **4***, 457.

31. Hahn, C., Song, S. H., Oh, C. H., & Berini, P. (2015). Plasmonic gain in long-range surface plasmon polariton waveguides bounded symmetrically by dye-doped polymer. *Applied Physics Letters* ***107***, 121107.

32. Tredicucci, A., Gmachl, C., Capasson, F., Hutchinson, A. I., Sivco, D. L., & Cho, A. Y. (2000). Single-mode surface plasmon laser. *Lasers and Electro-Optics*, (pp. 266-267). CLEO.

33. Jetté-Charbonneau, S., & Berini, P. (2007). External cavity laser using a long-range surface plasmon grating as a distributed Bragg reflector. *Applied Physics Letters* ***91***, 181114.

34. Oulton, R. F., Sorger, V. J., Zentgraf, T., Ma, R.-M., Gladden, C., Dai, L., . . . Zhang, X. (2009). Plasmon lasers at deep subwavelength scale. *Nature Letters* ***461***, 629.

35. Keshmarzi, E. K., Tait, R. N., & Berini, P. (2014). Near infrared amplified spontaneous emission in a dye-doped polymeric waveguide for active plasmonic applications. *Optics express* ***22***, 12452.

36. Keshmarzi, E. K., Tait, R. N., & Berini, P. (2012). Long-range surface plasmon single-mode laser concepts. *Journal of Applied Physics* ***112***, 063115.

37. Polyanskiy, M. (2008-2016). *Refractive index info*. Retrieved from Refractive index info: http://refractiveindex.info/?shelf=organic&book=poly%28methyl_methacrylate%29&page=Beadie